frontiers in Physics

REVIEW
published: 17 February 2022
doi: 10.3389/fphy.2022.791145

Ultrasound Contrast Imaging: Fundamentals and Emerging Technology

Hossein Yusefi[1] *and Brandon Helfield*[1,2]*

[1]Department of Physics, Concordia University, Montreal, QC, Canada, [2]Department of Biology, Concordia University, Montreal, QC, Canada

The development of microbubble contrast agents has broadened the scope of medical ultrasound imaging. Along with dedicated imaging techniques, these agents provide enhanced echoes from the blood pool and have enabled diagnostic ultrasound to assess and quantify microvascular blood flow. Contrast-enhanced ultrasound is currently used worldwide with clinical indications in cardiology and radiology, and it continues to evolve and develop through innovative technological advancements. In this review article, we present an overview of the basic microbubble physics and bubble-specific imaging techniques that enable this modality, and follow this with a discussion on new and emerging applications.

Keywords: microbubbles, contrast enhanced ultrasound, imaging, nonlinear scattering, subharmonic, ultrasound localization microscopy, super resolution, harmonic

OPEN ACCESS

Edited by:
Federico Giove, Centro Fermi—Museo Storico della Fisica e Centro Studi e Ricerche Enrico Fermi, Italy

Reviewed by:
Mehmet Burcin Unlu, Boğaziçi University, Turkey
Heikki Juhani Nieminen, Aalto University, Finland

***Correspondence:**
Brandon Helfield
brandon.helfield@concordia.ca

Specialty section:
This article was submitted to Medical Physics and Imaging, a section of the journal Frontiers in Physics

Received: *08 October 2021*
Accepted: *26 January 2022*
Published: *17 February 2022*

Citation:
Yusefi H and Helfield B (2022) Ultrasound Contrast Imaging: Fundamentals and Emerging Technology. Front. Phys. 10:791145. doi: 10.3389/fphy.2022.791145

1 INTRODUCTION

Ultrasound imaging is a well-established clinical tool for the morphological assessment of soft tissues, employed frequently in obstetrics, cardiology, and radiology [1]. As an ultrasonic wave (which is a longitudinal wave) is transmitted into the body, reflections are generated from tissue interfaces that are characterized by different acoustic properties, i.e., speed of sound and density. These scattered signals are recorded by the same transmitting transducer and used to generate an image. At typical diagnostic frequencies (≈1–10 MHz), the intrinsic scattering from the blood pool, however, is typically several orders of magnitude lower than tissue due to the size and properties of red blood cells [2]. Consequently, blood appears dark on conventional ultrasound images and blood flow characteristics cannot be readily assessed. For larger vessels, the relative motion of red blood cells compared to the surrounding tissue can be exploited to assess blood velocity using Doppler techniques [3], a strategy employed in many clinical applications (e.g., obstetrics [4], assessment of peripheral artery disease [5], cardiology [6]). This technique has limitations however when dealing with regions of slow blood flow, large tissue motion and/or low hematocrit percentage [1, 7].

Ultrasound contrast agents comprise of a suspension of small spheres of gas with a low solubility in blood (e.g., perfluorocarbon), typically ranging in size from below 1 to 8 μm in diameter. Unlike contrast agents used in other modalities, such as MRI and CT, the relatively large size of ultrasound contrast agents ensures that they remain strictly intravascular and act as red blood cell tracers [8]. Due to the compressibility of their gas cores, microbubbles vibrate about their equilibrium radius in an ultrasound field and possess scattering cross-sections several orders of magnitude higher than a solid particle of the same size [9]. The bubbles are stabilized by a thin bio-compatible encapsulation layer—typically a phospholipid monolayer, to

TABLE 1 | Current clinical contrast agent microbubbles, their salient characteristics, and their approved uses.

Name	Gas core	Shell material	Conc. (10^9 bub/ml)	d_N (μm)	d_V (μm)	f_{res} (MHz)	Approved uses	Region	Company
Definity (Luminity)	C_3F_8	DPPA, DPPC, MPEG5000 DPPE	8–13 [190–192]	<1.0 [190, 193]	6–8 [190, 191, 193, 195]	~10 [190, 191, 193, 195]	-LVO/EBD (adults)	United States, Canada, Europe, India, NZ, Australia	Lantheus
Lumason (Sonovue)	SF_6	DPSC, DPPG-Na, palmitic acid	0.1–0.5 [192]	1.5–2.5 [196]	6 [197]	~2 [197]	-LVO/EBD (adults and pediatric patients) -Characterization of liver lesions (adults and pediatric patients) -Evaluation of suspected or known vesicoureteral reflux (pediatrics)	United States, Canada, Europe, China, Brazil	Bracco
Optison	C_3F_8	Albumin	2–8 [192, 198]	3–4.5 [50, 192]	6–7 [50, 192]	2–4 [198]	-LVO/EBD (adults)	United States, Europe	GE
Sonazoid	C_4F_{10}	Hydrogenated egg phosphatidylserine sodium, sucrose	1.2 [199]	2.1 [192, 199]	2.6 [199]	4–6 [200]	-Myocardial perfusion -Living imaging -Focal breast lesions	Japan, South Korea, China, Norway, Taiwan	Daiichi-Sankyo/GE

offer a sufficient compromise between bubble vibration flexibility and resistance to dissolution *in-vivo* over timescales relevant for imaging, e.g., half-lives of minutes [10, 11].

Microbubble suspensions, typically on the order of 10^9 bubbles/ml, are injected intravenously into a peripheral vein in the arm [8], with a whole-body dose ranging from 0.2 to 2 ml [12]. There have been millions of diagnostic injections of contrast agent microbubbles worldwide [12], and they are accompanied by an excellent safety profile. Recent meta-analysis surveying microbubble tolerance indicates that the dominant cause of severe adverse effects is pseudoanaphylaxis (CARPA), with an estimated rate on the order of 0.004%–0.009% [13]. This rate is comparable to most analgesics and antibodies (0.005%–0.015% [14]), and similar if not lower than for other contrast imaging agents, e.g., CT with a rate of 0.04% [15], MR with a rate of 0.002%–0.005% [16, 17]. **Table 1** lists the clinical contrast agents, along with details on their salient characteristics and clinically approved applications. Microbubbles are approved in over 70 countries, predominately for cardiac applications, whereby their strong echo signal in the heart chambers improves left ventricular opacification (LVO). Recently, Lumason™ was approved for liver imaging and in various pediatric applications [18]. Aside from the clinical uses listed here, microbubbles are currently in use worldwide in many off label clinical imaging applications, including assessment of microvascular perfusion (e.g., myocardial [19], angiogenesis imaging [20]), imaging of the carotid to assess vascular stenosis [21] and plaque stability [22], lesion and flow characteristics in the abdominal region [23, 24], breast lesion detection [25], evaluation of inflammatory bowel disease [26], and assessment of ovaries [27], prostate [28] and thyroid [29].

In this review, we present an overview of this established yet evolving imaging modality. First, we present a brief summary of the fundamental physics of microbubble behaviors that are critical for the effectiveness of this approach, followed by an introduction to the main conventional pulse sequences that are designed to exploit these behaviors to generate bubble-specific images. Next, we discuss exciting advancements in the techniques and applications of ultrasound contrast imaging, including the development of emerging contrast agents, novel imaging and image analysis techniques, and the implementation of contrast ultrasound as a therapy monitoring technique. Note that this is not a comprehensive review, rather an overview of the critical work that has defined this modality and salient investigations into new and ground-breaking applications.

2 ULTRASOUND-MICROBUBBLE INTERACTIONS

A gas-filled microbubble vibrates when traversing through an acoustic beam, contracting and expanding about its equilibrium radius R_0. Almost all the current models that explain the oscillation dynamics of a bubble have their origin in Rayleigh-Plesset-type equations [30], which describe the radial motion of an isolated, unencapsulated bubble. This equation, which only incorporates spherical vibrations, can be derived by applying Newton's third law to the surface of a bubble and equilibrating the pressure on the bubble wall from the gas inside and the surrounding fluid media outside, resulting in the following equation:

$$R\ddot{R} + \frac{3}{2}\dot{R}^2 = \frac{1}{\rho}\left[P_{G0}\left(\frac{R_0}{R}\right)^{3\gamma} + P_v - \frac{2\sigma}{R} - 4\eta_L\frac{\dot{R}}{R} - P_0 - P_{ac}(t)\right], \quad (1)$$

where R is the radius of the bubble, ρ is the density of the liquid, $P_{G0} = P_0 - P_v + 2\sigma/R_0$ is the pressure inside the bubble with P_0 the atmospheric pressure, P_v the vapor pressure inside the bubble and σ is the surface tension at the gas-liquid interface, γ is the

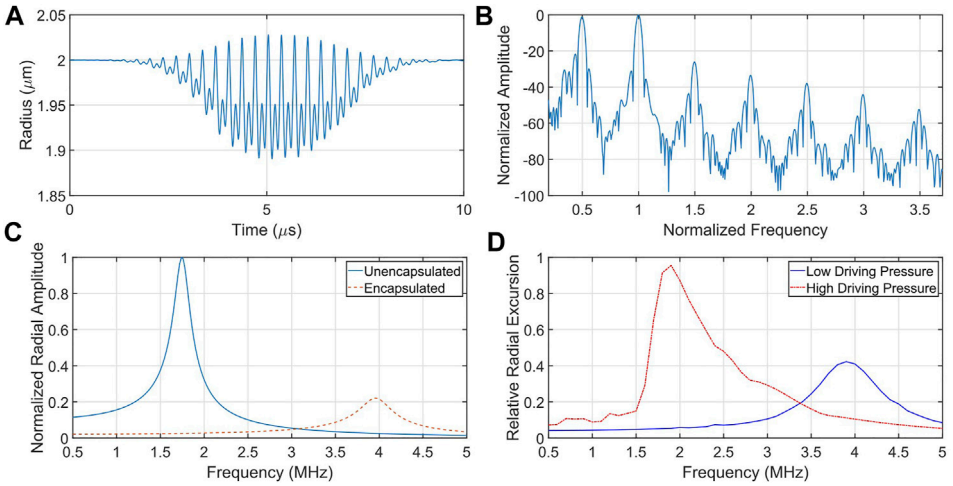

FIGURE 1 | Illustrative microbubble simulations depicting its resonant and nonlinear behaviour. **(A)** Radius versus time of an oscillating microbubble and **(B)** it is corresponding frequency content. Note the presence of subharmonic (0.5), ultraharmonic (1.5, 2.5, 3.5) and harmonic (2, 3) energy, as well as energy at the fundamental frequency band (1). **(C)** The presence of an encapsulating shell serves to increase the resonance frequency and dampen the vibrational amplitude of an otherwise identical microbubble. **(D)** Under large forcing conditions, microbubbles exhibit asymmetrical resonance, including a shift down in resonance frequency with increasing forcing amplitude. Note here the inherent skewing of the resonance response, typical of a strain-softening resonator.

polytropic exponent of the gas; η_L is the dynamic viscosity of the liquid; P_{ac} is the driving acoustic pressure due to the ultrasound field and dots denote differentiation with respect to time. From fundamental fluid dynamic principles, including conversation of mass and momentum, the microbubble scattered pressure P_{sc} due to its vibration can be approximated by

$$P_{SC} \approx \rho \frac{\ddot{R}R^2 + 2R\dot{R}^2}{r}, \tag{2}$$

where r is the observational distance from the bubble surface. In the context of ultrasound imaging, bubble activity is commonly separated into two acoustic regimes that give rise to distinct spectral features. Under low amplitude driving conditions at frequency f, microbubbles undergo periodic oscillations about their equilibrium size resulting in echoes that possess a rich resonant structure, exhibiting energy at harmonic (nf, $n = 2, 3 \ldots$), sub-harmonic ($f/(n+1)$, $n = 1, 2, \ldots$) and ultra-harmonic ($(2n+1)f/2$, $n = 1, 2 \ldots$) frequency bands (**Figures 1A,B**). This type of cavitation is called stable (or non-inertial) cavitation, which is typically desired in routine contrast examinations. When the acoustic pressure is increased above a threshold value, microbubbles can rapidly expand and collapse during the compression phase of the ultrasound wave resulting in a transient, high-amplitude echo characterized by broadband emissions. As this bubble collapse is dominated by the inertia of the surrounding fluid, it is often referred to as inertial cavitation [31]. Quantitative indicators of inertial cavitation on an individual microbubble scale have been suggested, including when the maximum bubble radius $R_{max} \geq 2R_0$ otherwise known as the Flynn criteria [32]. The disruption of microbubbles results in an immediate loss of gas and thus in a time-dependent loss of contrast signal. On clinical scanners, the mechanical index $MI = P/\sqrt{f}$, where P is the peak-negative pressure amplitude in MPa and f is the centre frequency in MHz, is a metric used to estimate the likelihood of inertial cavitation and is generally maintained at low values to minimize bubble destruction [33]. Indeed, across the broad spectrum of all clinical contrast imaging applications, it is recommended to start at the manufacturers default contrast MI. If perfusion is still not well visualized after exhausting other image-enhancing strategies (e.g., receiver gain), then the MI should be increased by the smallest increment allowed on the given clinical system [18], with a maximum recommended MI between 0.2–0.3 [34–36]. However, specific techniques have been developed (e.g., disruption-replenishment [37, 38]) whereby short duration, large MI pulses (e.g., high MI flash under the FDA limit of MI = 1.9) are employed to purposefully disrupt microbubbles in the focal volume, followed by a rapid switch back to low MI imaging pulses. The rate at which these bubbles replenish the imaging plane can be used to assess blood flow characteristics upon application of relatively simple models [37, 38]. The specific MI that elicits microbubble disruption has been the subject of much investigation [39–43] and has been shown to be dependent on microbubble formulation, size, and surrounding environment.

Ultrasound-driven microbubble response is resonant in nature, and the resonance frequency is one of the important factors in agent design and optimization. Under low acoustic driving conditions, the nonlinear equation of motion **Eq. 1** can be reduced to one of a harmonic oscillator with a linear resonance frequency f_0 given by:

$$f_0 = \frac{1}{2\pi}\sqrt{\frac{3\gamma P_0}{\rho R_0^2} + \frac{2\sigma(3\gamma - 1)}{R_0^3}}, \tag{3}$$

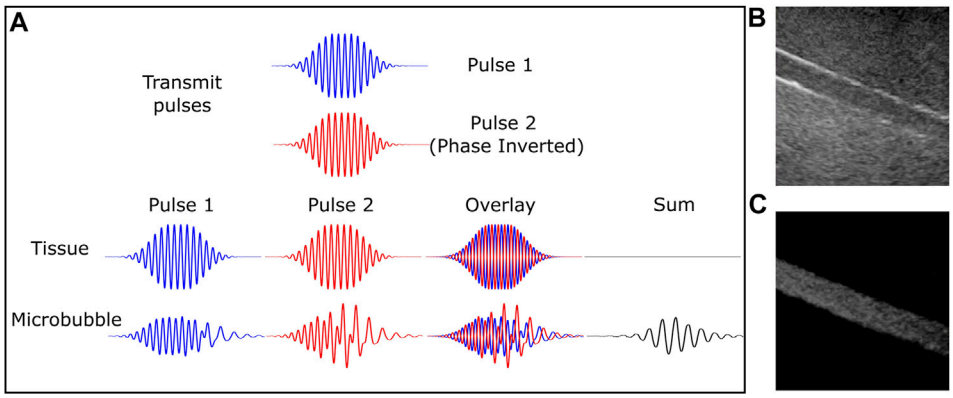

FIGURE 2 | Microbubble-specific imaging sequences capture nonlinear signal from contrast agent while rejecting linear scattering tissue. **(A)** Schematic diagram depicting the pulse inversion technique. Two pulses that are 180° out of phase will result in tissue echoes that are similarly out of phase. However, this is not the case for microbubbles due to their nonlinear behavior. The summed echo results in near complete cancellation for linear tissue and significant signal from echoes generated from microbubbles. **(B)** B-mode and **(C)** contrast-specific imaging of an 8 mm vessel phantom highlights the increased vessel contrast due to microbubble-specific imaging. This was acquired with a Philips iU22 scanner using a C5-2 probe and Definity™ contrast agent.

where an inverted relationship between resonance frequency and size can be observed.

The addition of an encapsulating shell has led to adjustments of **Eq. 1**, which incorporate the viscoelastic properties of the thin shell, i.e., shell stiffness and viscosity. While many models have been developed to capture various aspects of microbubble physics, under low-amplitude transmit pressure conditions they are all in agreement with experimental observations which confirm that the encapsulating layer serves to increase the resonance frequency and the vibration dampening of an otherwise identical bubble (**Figure 1C**). As driving amplitudes increase, microbubbles display nonlinear resonance phenomena, including strain-softening behavior resulting in asymmetric resonance curves shifting to lower resonance frequencies [44, 45] (see **Figure 1D**). While these nonlinear behaviors can be generated by unencapsulated gas bubbles [46], the surface rheology of the encapsulation material at megahertz oscillations plays a key role in amplifying these effects [47]. As such, there have been extensive efforts to understand the underlying physics of encapsulated microbubble vibration dynamics, including asymmetric oscillations [48], nonlinear resonance [49], multiple scattering [50], and boundary effects [51].

3 CONTRAST PULSE SEQUENCES

Nonlinear behavior of vibrating microbubbles is central to their effectiveness as an ultrasound contrast agent. These emissions provide a means to separate bubble signals within small vessels from those of the surrounding (approximately linear) tissue (**Figure 2**). Original methods of bubble detection consisted of harmonic imaging, whereby energy at the second harmonic (twice the driving frequency) was collected and filtered from the receive signal. Since microbubbles generate much larger second harmonic signal than tissue, this results in better signal-to-noise ratios than that from the fundamental energy. This approach however requires long-duration (narrowband) transmit pulses in order to ensure separation of the spectral components at f and $2f$, as well as to fit within the transducer bandwidth. These conditions result in decreased axial resolution and ultimately a trade-off between image resolution and contrast quality. Multi-pulse contrast imaging pulse sequences, consisting of pulse inversion (PI [23]), amplitude modulation (AM [52]) and combinations thereof (contrast pulse sequences, CPS [53]), have been developed to circumvent these issues to specifically image the blood pool with high specificity and sensitivity. The following sections briefly outline these two main approaches; for a more exhaustive survey of microbubble-specific imaging methods, the reader is referred to a recent review article [54].

3.1 Pulse Inversion

The generalized scattered signal from a scatterer $O(x(t))$ can be modeled by a polynomial expansion:

$$O(x(t)) = \sum_{m=1}^{\infty} a_m x^m, \tag{4}$$

where $x(t)$ is the transmit waveform. The contributions of the nonlinear components are defined by the coefficients a_m, whereby for linear systems only a_1 is nonzero. As ultrasound pulses consist of sinusoidal transmit sequences, e.g., $x(t) = \cos(\omega t)$ with $\omega = 2\pi f$ the angular transmit frequency, the nonlinear echo can be approximated by

$$O(x(t)) \approx a_1 \cos(\omega t) + \frac{a_2}{2}[1 + \cos(2\omega t)] + \frac{a_3}{4}[\cos(\omega t) + \cos(3\omega t)] + \frac{a_4}{8}[3 + 4\cos(2\omega t) + \cos(4\omega t)] + \ldots \tag{5}$$

Note from the above equation that even-order terms create echoes at even harmonics (and DC), while the odd-order terms account for echoes at the fundamental frequency and odd-order

harmonics. The pulse inversion multi-pulse sequence consists of sending in two transmit pulses that are 180° out of phase with each other (**Figure 2A**). Upon summation of the resulting echoes $s(t)$, the linear contributions are removed and only even order harmonic signal is retained:

$$s(t) = O_1(x(t)) + O_2(-x(t)) = 2\sum_{m=1}^{\infty} a_{2m}x^{2m}. \quad (6)$$

While this technique suppresses fundamental signal, it still requires careful selection of transmit frequency to be able to sensitively detect even order harmonics with the given transducer.

3.2 Amplitude Modulation

In a similar attempt to preserve nonlinear contributions, amplitude modulation consists of transmitting a sequence of pulses that are scaled by a constant factor. Typically, the echoes received from $x_1(t)$ and $x_2(t) = \frac{1}{2}x_1(t)$ (referred to as "full amplitude" and "half-amplitude" pulses respectively) are scaled and subtracted, resulting in a residual signal $s(t)$ defined as:

$$s(t) = O_1(x_1(t)) - 2O_2\left(\frac{1}{2}x_1(t)\right). \quad (7)$$

This results in a signal that partially retains all harmonics, including signal at the fundamental frequency; shown here to third order:

$$s(t) \approx \frac{a_2}{4}[1 + \cos(2\omega t)] + \frac{3a_3}{16}[\cos(\omega t) + \cos(3\omega t)] + \ldots \quad (8)$$

It is important to note here that the signal component within **Eq. 8** at the driving frequency ω represents the scaled difference in the fundamental component due to different amounts of nonlinear signal in the two driving pulses. This "nonlinear fundamental" signal results from the fact that microbubbles exhibit nonlinear resonance characteristics, specifically an amplitude dependent resonance frequency (**Figure 1D**). As such, the fundamental microbubble response will not necessarily be linearly proportional to the input transmit pressure, e.g., the response from $x(t)$ will not be twice that of $\frac{1}{2}x(t)$. Indeed, bubble-specific strategies are currently under development that exploit the accompanying echo phase lag associated with this phenomenon [55]. While this approach retains less even-order harmonic energy than PI, the residual "nonlinear fundamental" is particularly useful as it can be well detected within the transducer bandwidth.

Both PI and AM methods can be performed using three or more pulses, offering some advantages in tissue rejection at the cost of temporal resolution. The combination of these two approaches (PIAM, or CPS) retains similar levels of odd-order nonlinear energy as AM while preserving more even-order harmonics, albeit less than the PI technique alone.

4 EMERGING TECHNOLOGIES

Contrast-enhanced ultrasound imaging is employed in many clinically approved and off-label applications worldwide. Cutting-edge advancements in this area are being made simultaneously on many fronts, including contrast agent synthesis, the design of novel pulse sequences and image processing techniques, device development, and on the development of remote monitoring for ultrasound therapeutics (**Table 2**).

4.1 Contrast Agents

Microbubbles are currently the only clinically approved ultrasound contrast agent. One of the strengths of these bubbles is that they remain intravascular due to their size, allowing for diagnostic measurements that would be otherwise difficult with diffusible tracers. However, there is a growing focus to extend the use of these 'traditional' ultrasound contrast agents towards other applications, including molecular-based imaging, imaging of the extravascular space, and as a dual imaging and therapeutic delivery platform.

4.1.1 Molecularly Targeted Microbubbles

Non-invasive imaging of pathophysiological events has recently been shown feasible with ultrasound due to the synthesis of functionalized microbubbles [56], i.e., microbubbles with one or more targeting moieties incorporated into the phospholipid encapsulation [57]. Due to the strictly intravascular nature of microbubbles, target sites have aimed at processes that occur within the vasculature, such as inflammation [58], angiogenesis [59], and thrombus formation [60]. This technique has shown significant pre-clinical promise, with agents synthesized to target key endothelial biomarkers involved in disease, e.g., ICAM-1 [61], VCAM-1 [58], $\alpha_V\beta_3$ [62], E-selectin [63]. Clinical trials to assess safety and tumor detection sensitivity have shown encouraging results using microbubbles functionalized for vascular endothelial growth factor receptor 2 (VEGFR2) in ovarian, breast and prostate cancer [64, 65]. Indeed, this technique can be used as a means for early differential disease detection, as pathological molecular expression often occurs at an earlier timepoint in relation to anatomical changes—but it can also be used as a tool for non-invasive therapy monitoring [66]. In either case, the objective is to establish a proportional relationship between detected bound bubble signal and the level of target molecule expression. Part of this strategy is therefore to preferentially detect signals from bound bubbles, as distinct from freely circulating, or non-bound stationary agent. While there have been some suggestions of novel echo characteristics that would specifically indicate a bound versus unbound bubble [67, 68], imaging techniques to exploit this behavior are not yet used robustly in practice. Instead, a number of approaches have been developed to estimate adherent bubble signal, one of which is to exploit the increased persistence of bound bubbles. Exploiting the relatively short half-life of freely circulating microbubbles, image acquisition ~10 min post injection will preferentially capture bound bubble signal [69]. Another strategy is to first acquire a baseline image consisting of all bubbles (both bound and unbound) and to apply a large magnitude pulse to disrupt them [56]. Contrast images are then acquired immediately post-disruption to monitor the reperfusion of circulating microbubbles into the imaging plane. The bound-bubble

TABLE 2 | Summary of emerging ultrasound-microbubble based techniques. See text for references and further details.

Emerging technology/ Technique	Concept	Applications
New contrast agents	To design novel acoustically-sensitive agents that allow for the extraction of diagnostic information otherwise impossible with standard microbubble contrast agents	*Targeted microbubbles*: Molecular imaging of vascular-based markers of disease (e.g., thrombosis, angiogenesis, ischemia) *Droplets/nanobubbles:* Extravascular imaging in cancer applications *Gas vesicles:* Acoustic reporter genes, environmentally-triggered acoustic reporters
Super-harmonic Imaging	To use higher order harmonic signal unique to microbubble vibrations to generate high contrast-to-tissue ratio contrast images	Tumor vasculature imaging
Non-invasive pressure estimation	To extract ambient pressure information from microbubble acoustic signatures	Portal vein hypertension, intra-cardiac measurements
Ultrasound Localization Microscopy	To use bubble localization information to generate images that surpass the diffraction limit	Tumor vasculature imaging, neurological
Microbubble-therapy monitoring	To extract qualitative and quantitative microbubble emission characteristics as a surrogate for therapeutic endpoints	Cardiovascular and cancer-based applications of focused ultrasound therapy, immunotherapy, and microbubble-mediated therapeutic delivery

specific image is then estimated as the difference between the pre- and post-burst images. A third approach is to exploit the increased decorrelation due to motion associated with circulating bubbles relative to stationary ones. While this has shown significant promise in pre-clinical testing [70], it is expected to have limitations in regions of substantial tissue motion.

Despite the relative success of the aforementioned bound bubble quantification techniques, only a small fraction the injected microbubbles bind to the activated endothelium, on the order 1–2% [71]. A clever approach to increase the number of microbubbles that make direct contact with the endoluminal border is through the use of acoustic radiation force, originally postulated for such a purpose over two decades ago [72, 73]. Acoustic radiation forces, otherwise known as Bjerknes forces, are the forces imparted to a small object within an acoustic beam by the acoustic wave [7]. In the context of ultrasound-stimulated microbubbles, the primary Bjerknes force magnitude F directed away from the transducer experienced by a resonating microbubble in a pulsed field of duty cycle D and pulse repetition interval T can be estimated as [74].

$$F = \frac{P^2 R_0}{\delta \rho c f_0}\left(\frac{D}{T}\right), \tag{9}$$

where δ is the damping coefficient [75] and c is the speed of sound. Secondary Bjerknes force, which is the force ascribed to the translational dynamics between two vibrating microbubbles, can also be shown to be highly dependent on microbubble size and separation distance [74]. While the physical acoustics of these phenomena have long been investigated [76, 77], it has been since utilized as an approach to increase microbubble binding efficiency [74, 78, 79]. Quantification of acoustic radiation force (ARF)-enhanced microbubble imaging can be performed using a relative measure of bubble signal pre- and post-ARF burst, allowing for an attenuation-independent measure of quantification (i.e., one that does not rely on the absolute signal intensity) [80, 81].

4.1.2 Sub-Micron Contrast Agents

Motivated by the enhanced-permeability and retention effect [82], whereby small nanometer sized particles locally extravasate from leaky blood vessels and accumulate in the perivascular space of solid tumors, there are numerous ultrasound-sensitive sub-micron agents currently under investigation. These mainly include phase-shift droplets [83], nanobubbles [84], gas vesicles [85], echogenic liposomes [86], and polymeric nanoparticles [87]. Perhaps the most well-studied of these are volatile, phase-shift sub-micron droplets synthesized from perfluorocarbons (PFCs). As a liquid, droplets provide limited acoustic contrast and are generally not detectable with conventional ultrasound. However, under externally applied ultrasound conditions, these droplets can be acoustically vaporized into detectable, micrometer-sized bubbles approximately 5–10 times their precursor size [91]. Droplet compositions generally consist of PFCs due to their low toxicity, low solubility and their boiling points near physiological temperatures [83], allowing the design of droplets in or near a superheated state. As these superheated droplets are thermodynamically unstable, they are stabilized through phospholipid encapsulation—reducing surface tension and inhibiting diffusion of the PFC into the surrounding medium. Indeed, droplets can be synthesized directly from pre-cursor microbubbles, e.g., commercially employed agents such as Definity™ [88, 89]. While the physics of acoustic droplet vaporization is still an active area of research, the process likely involves both intrinsic (e.g., PFC, encapsulation material) and extrinsic (e.g., sound and its propagation medium) factors. The vaporization threshold of individual droplets empirically exhibits a size-dependence, with larger, micron-sized droplets requiring lower pressures to vaporize [90–92]. Further, there is an increasing threshold with decreasing frequency [93]—indeed these two factors make the vaporization of small, sub-micron droplets at clinically relevant frequencies a challenge. However, recent translational studies using pre-clinical and programmable array systems have

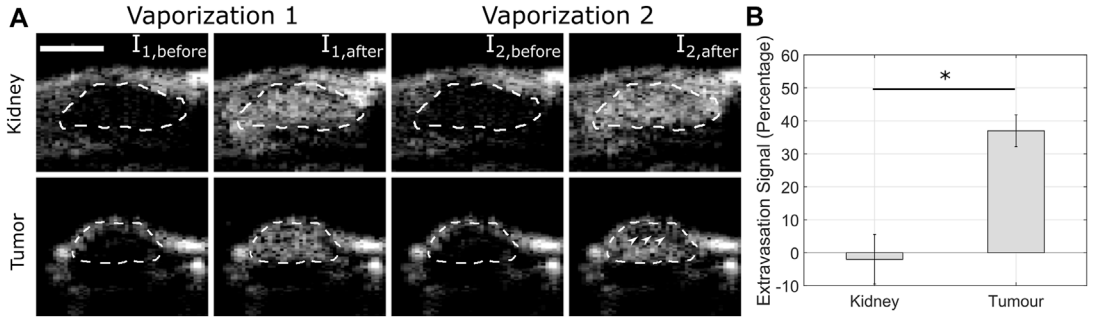

FIGURE 3 | Estimated droplet extravasation signal is larger in tumor than in kidney. **(A)** Two successive vaporization sequences (Vaporization 1 and 2) separated by 30 s were transmitted to both the kidney (highly intravascular organ) and tumor xenograft (intravascular and extravascular components) in a mouse model, outlined in the dashed lines. The white arrowheads denote the lack of signal enhancement from the second vaporization pulse within the tumor, suggesting droplet extravasation. Scale bar is 5 mm. **(B)** Quantification of extravasation signal ($p < 0.001$). Reprinted by permission of Elsevier from Helfield et al Ultrasound and Medicine and Biology, 2020 [94], see the reference for more details.

shown the feasibility of *in-vivo* image-guided vaporization and extravascular imaging [94, 95], see **Figure 3**.

As an alternative to phase-shift low-boiling point droplets, recent studies have begun to explore nanobubble contrast agent, typically on the order of several hundred nanometers in size [96]. According to classical models (e.g., **Eq. 1** and **Eq. 3**), nanobubbles are not expected to undergo significant vibrations and scattering at clinically relevant frequencies (e.g., 1–10 MHz). However, studies have demonstrated scattered emissions from nanobubbles at both low [97, 98] and high frequencies [99]. The increased concentration of nanobubbles per unit volume may compensate for the weak scattering from an individual nanobubble, and bubble coalescence (multiple nanobubbles combining to form a microbubble) may also play a role in the observed signal. In addition to these aspects, recent surface modifications (surfactants, e.g., Pluronic) to nanobubble encapsulation layers has been suggested as a potential mechanism to further reduce surface tension and increase flexibility [96, 97]. Regardless of the mechanism, observations of intact nanobubbles in the extravascular space have very recently been documented [100, 101].

Recently, a new and exciting type of biologically-derived, sub-micron ultrasound contrast agent has been developed by harnessing gas vesicles (GVs) [85]. These vesicles, which were originally identified within gas vacuoles of cyanobacteria, function natively to regulate cellular buoyancy for optimal exposure to light and nutrients [102]. GVs are inert, hollow, gas-filled structures formed entirely from protein. The main consistent is a small protein (GVpA) arranged in a linear crystalline array along ribs that form the GV shell and conical caps. A second protein (GVpC) adheres to the outside of the ribs and stabilizes the structure. These vesicles are freely permeable to gases and liquid water is kept out due to surface tension at the hydrophobic inner surface. GVs have been found in many prokaryotes (e.g., bacteria and archaea), and extensive research has concluded that these GVs possess similar morphology and are constructed from a homologous protein. The size and shape of GVs is a function of the species that generate them, but they are typically cylindrical or spindle-liked shaped, with lengths ranging from 0.1 to 2 μm and widths between 45–200 nm [103]. While similar in principle to other pre-formed sub-micron agents, GVs are rigid, non-spherical structures. In the pioneering work by Shapiro et al [85], purified GVs generated from *Halobacterium salinarum* (Halo) produced robust contrast using a pre-clinical scanner, including nonlinear harmonic content *in-vitro* and in mouse liver using an amplitude modulation pulse sequence (e.g., **Eq. 7**). Since then, many experimental and theoretical investigations have confirmed that GVs are able to elicit nonlinear signal and acoustically-mediated collapse *in vitro* and *in-vivo* [104, 105], which highlight the potential of GVs to serve as background-subtracted imaging agents. However, perhaps the greatest differentiator between GVs and traditional ultrasound contrast agents is their ability to be genetically modified. Indeed, the acoustic properties of GVs can be modified at the level of their constituent proteins [106], which enables the concept of environmentally-modulated nonlinear contrast signal (e.g., detecting the presence of specific proteases [107]). Further, recent work has demonstrated the capacity of GVs to act as an acoustic reporter gene in mammalian cells (e.g., an acoustic version of an optical reporter like green-fluorescent protein), whereby contrast signal can be correlated to genetic expression [108].

4.2 Super-Harmonic Imaging

As microbubble vibrations possess a rich resonant structure (**Figure 1B**), there have been recent developments towards generating contrast images using microbubble super-harmonic frequency components, defined as third-order harmonics and higher (nf; $n = 3, 5, 6 \ldots$). An extension of traditional second harmonic imaging techniques, the selective reception of these higher-frequency signals results in higher image resolution and contrast-to-tissue ratios compared to standard contrast imaging sequences. Due to the bandwidth of standard clinical transducers, which limits its ability to transmit and receive signals at both the fundamental and super-harmonic energy bands, the implementation of this approach requires multiple, independent transducer elements. This can be accomplished by designing novel phased arrays with interleaved elements for

transmit and receive [109, 110], and confocally aligned dual-element transducers [111, 112]. Recent incarnations of this approach, termed acoustic angiography [113], performs super-harmonic imaging using transmit frequencies between 2–4 MHz and receives echo signal from 25–30 MHz. Using this device, an *in-vivo* resolution of 150–200 μm and a contrast-to-tissue ratio of 20 dB has been demonstrated [114, 115]. To date, this technology has been employed to image and assess tumor microcirculation [116, 117] and remains mostly pre-clinical; although very recent work highlights its potential for clinical translation [118, 119] and is currently an active area of research.

4.3 Non-Invasive Pressure Estimation

Local blood pressure estimation provides valuable clinical information on the physiology of many organs, and can be employed in the diagnosis of disease in the heart and kidneys. Most current clinical techniques to assess blood pressure within non-limb vessels use catheter-based manometers, which is an invasive approach and introduces changes to the local blood circulation and thus the blood pressure. Perhaps one of the most impactful applications of non-invasive pressure estimation would be for the early detection of clinically significant portal vein hypertension, defined as an increase in the pressure gradient between the portal vein and hepatic veins exceeding 10 mmHg [120]. As noted almost four decades ago [121], bubble response is a direct function of the ambient hydrostatic pressure and may, in principle, be used as a pressure sensor to detect fluctuations in local blood pressure. An increase in ambient pressure effectively compresses the microbubble, resulting in a shift upwards in resonance frequency. For a given transmit frequency, this will manifest itself in the amplitude of the resulting scattered echo. These original works performed on unshelled bubbles resulted in large uncertainties (as much as 30%, or 50 mmHg compared to reference standards [122]) due to the challenge of detecting the relatively small shift in resonance frequency (~1 kHz shift from a change in 10 mmHg). While the rheological characteristics of phospholipid encapsulated microbubbles results in much larger resonant shifts (~0.07–0.24 MHz per 10 mmHg [123]) that may be sufficiently detectable for clinical utility, major advances in this application of remote blood pressure estimation are derived from investigations into the modulation of subharmonic scattering. Based on earlier works on commercially available contrast microbubbles that indicate a decrease in subharmonic scattering with increasing hydrostatic pressure [124], subharmonic-aided pressure estimation efforts (referred to as SHAPE [125]) have met initial success in pre-clinical models [126, 127] and in clinical trials for portal hypertension [128] and intra-cardiac measurements [122].

4.4 Ultrasound Localization Microscopy

A flourishing research area within diagnostic ultrasound is the development, implementation and interpretation of ultrafast ultrasound imaging, in which up to 20 kHz frame rates (compared to 10–100 Hz using conventional scanners) can be achieved through advances in hardware and software. This concept is based off the transmission of an ultrasonic plane wave (i.e., unfocused beam), which avoids the time-consuming process of sequential scanning and beamforming conducted by traditional focused-mode imaging. The echoes from a single plane wave transmission are received by the transducer elements and subsequently processed and beamformed in parallel. While the use of a single, unfocused transmit beam results in poor image resolution, SNR can be markedly increased by transmitting multiple plane waves at different angles and compounding the coherent beamformed images. Despite this slight subsequent reduction in frame rate, this still results in a very fast acquisition relative to conventional focused beam, limited in principle only by the two-way speed of sound in tissue. Ultrafast plane wave imaging has opened an array of contrast and non-contrast ultrasound applications that take advantage of such increased temporal resolution, including ultrafast elastography [129], cardiac [130], and Doppler-based applications [131].

Perhaps the most disruptive technique derived from a microbubble-based application of this technology to date is ultrasound localization microscopy (ULM, see **Figure 4**) [132]. As a super-resolution imaging technique, it has begun a paradigm shift in biomedical ultrasound imaging applications despite many previous investigations into methods to improve ultrasound imaging resolution. In standard imaging techniques, image resolution is bound by diffraction to the scale of the wavelength; for example, in a 6-MHz ultrasound imaging system (λ = 250 μm), the diffraction limit is 125 μm ($\lambda/2$). The ULM approach exploits the localization of microbubbles to finely sample and image the microcirculation beyond the limit imposed by diffraction, showing impressive results in the areas of oncology [116, 133] and neurology [134, 135] that result in an improvement of the resolving power of ultrasound up to a factor of 10 compared to the diffraction limit [136, 137]. It is an approach inspired by the light microscopy counterpart; photoactivated localization microscopy (PALM) and stochastic optical reconstruction microscopy (STORM). These cutting-edge light microscopy techniques, which can image beyond the diffraction limit by an order of magnitude [138–140], rely on photoactivatable fluorescence probes that display unique spectral features upon exposure to different wavelengths of light. These reversible, "photo-switchable" probes in combination with fast-frame imaging cameras enable the rapid acquisition of frames in which only a subset of the sources is visible. With knowledge of the point-spread function of the imaging system, the collection of many sub-wavelength localizations can be reconstructed with resolution lower than the diffraction limit. Indeed, the development of these techniques was so important that it led to the attribution of the 2014 Nobel prize in Chemistry to Eric Betzig, Stefan Hell and William E. Moerner.

An ultrasonic version of super-resolution is achieved by replacing the fluorescent markers with microbubbles (which are sub-wavelength, individual acoustic sources), and the fast cameras with plane-wave, programmable ultrasound imaging systems. These programmable systems give access to the pre-beamformed time-domain data (RF data), whereby assuming a single source, the signal time delay τ as a function of array position x produced by a single microbubble echo propagating at a constant speed c is given by:

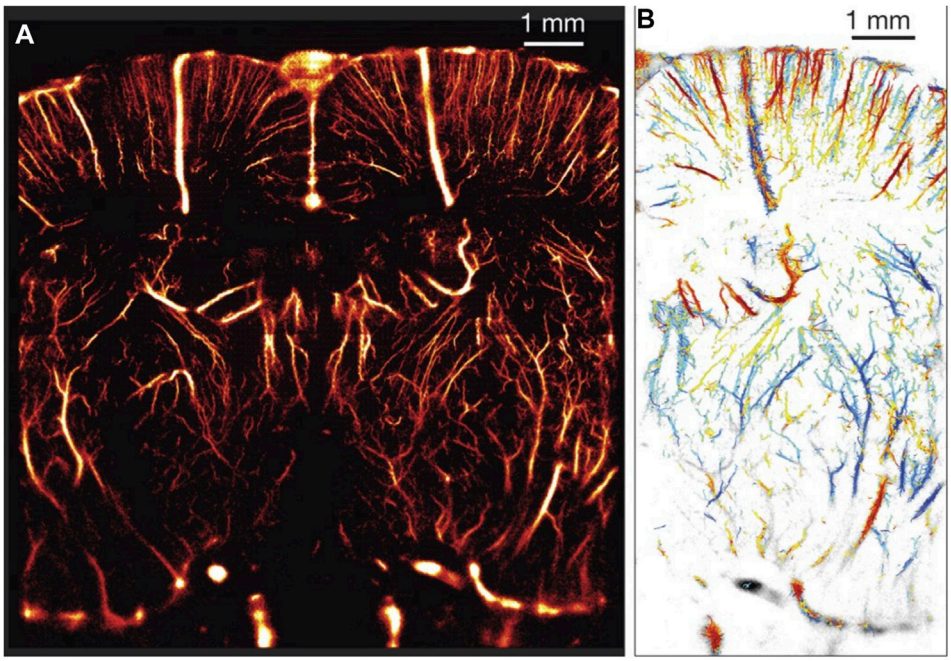

FIGURE 4 | (A) An example of ULM applied in a rat brain through a thinned, intact skull providing a resolution of 10 µm × 8 µm in depth and lateral direction, respectively. **(B)** In-plane velocity map from parts of the vessel from panel A. Scale bar runs from −14 mm/s (blue) to +14 mm/s (red). Reprinted from [135] with permission from the authors and Nature Publishing Group.

$$\tau = \frac{\sqrt{z_0^2 + (x - x_0)^2}}{c}, \tag{10}$$

where z_0 and x_0 are the depth and lateral position of the microbubble, respectively. One approach to microbubble localization is to fit this delay function (i.e., a parabolic function), the peak of which will provide the position of the microbubble at much higher resolution than the wavelength [132]. Alternatively, even on beamformed images acquired from conventional ultrasound scanners, various algorithms have been developed to estimate the intensity-weighted centroid of an individual microbubble and has shown success in dilute microbubble applications [141, 142].

The general concept of acquiring a super-resolution imaging using ULM will next be outlined here. After injection of a dilute suspension of contrast agent, video acquisition of the location of interest, either using B-mode or contrast-specific sequences, can be taken using either conventional beam or fast-frame plane wave techniques. Since the resulting ULM image is constructed point by point, a sufficient quantity of microbubbles is required to reconstruct the vasculature, on the order of 1 million events [135] depending on the vessel density and field of view. Given the relatively slow blood velocities in the microvasculature, this often requires long image acquisition times and results in a vast amount of data for processing. Motion correction algorithms are next applied to minimize motion-related localization artefacts, which present a particular challenge due to these long scan times. Various techniques have been demonstrated within the context of the ULM workflow, including phase-correlation approaches between successive B-mode images, all of which result in corrections on the order of hundreds of micrometers for in-plane motion [143–145]. While out-of-plane motion correction is not possible using this 2D approach, 3D ULM techniques are currently being assessed [146]. Following this, a microbubble-filtering processing step is introduced, which can include isolating nonlinear emissions [134, 141] as well as alternative image processing strategies including spatiotemporal-based filtering algorithms [135, 145, 147]. Microbubble localization is then performed by estimation of its centroid using either the raw RF data or the beamformed image. A critical challenge here is the reliable separation of one microbubble from another. The most direct way of localizing a single microbubble is to use a low concentration of contrast agent (e.g., 10^6 bubbles/ml) [134, 141, 148], which guarantees an inter-bubble spacing (e.g., 100 μm) of several imaging wavelengths at traditional transmit frequencies. Even in such instances, the robust SNR generated from an individual microbubble is of paramount importance, and will ultimately affect the ULM resolution. Recent work [149] has suggested that exploiting the phase response of vibrating microbubbles, a property linked to their resonant nature [75], can increase ULM image quality. However, there are emerging alternative strategies that allow for higher local doses of microbubbles, attempting to circumvent the spatial resolution versus acquisition time trade-off inherent to ULM. Increased local microbubble concentrations not only shorten the scan time, but increase the SNR. In order to overcome the overlapping of the point-spread functions, spatiotemporal filtering algorithms to separate overlapping microbubble signals [150, 151] have been introduced. Recently, algorithms based on deep learning (Deep-ULM) have been proposed, offering the advantage of acquiring high resolution images with high microbubble concentrations and lower

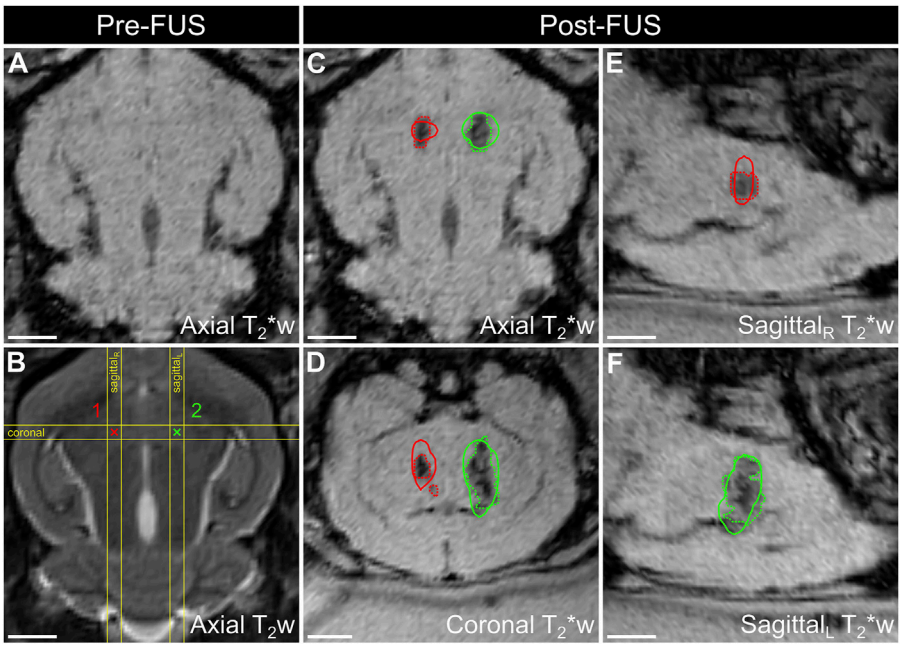

FIGURE 5 | Spatial correlation of ultrafast 3D microbubble cavitation with focused ultrasound (FUS) brain tissue damage in a rabbit model. Baseline T_{2^*w} **(A)** and T_{2w} MRI **(B)** images pre-sonication depict target locations for two focused ultrasound treatment conditions (labeled 1 and 2). Axial, coronal and sagittal T_{2^*w} MRI images immediately post-sonication [**(panels C–F)** respectively] depict hypointense regions indicative of tissue damage (dotted lines) overlaid by the corresponding spatial microbubble cavitation data (solid lines). The coronal and sagittal slice volumes are indicated in panel B (yellow lines). Scale bar = 5 mm. Figure modified from Jones et al *Theranostics*, 2020 [183] with permission from the authors.

computation load compared to other techniques. This AI-based approach is capable of learning the nonlinear image domain implications of overlapping point-spread functions originating from populations of closely spaced microbubbles [152]. Finally, tracking of microbubble trajectories, using simple or more complex algorithms [145, 153], allows not only for the estimation of super-resolved blood flow velocities [135, 144], but for improved image quality due to the fact that a single microbubble can reconstruct several pixels during its trajectory. Indeed, as adequate sampling of microbubble location is critical for the success of tracking algorithms, ultrafast imaging techniques offer a major advantage over conventional imaging approaches. Images are often then reconstructed by projecting the detected tracks on a sub-wavelength grid matrix. True estimates of vessel diameter, therefore, cannot rely on sparse tracks but require them in sufficient number to ensure mapping of the entire lumen, a track density determined by the width of the vessel divided by the super-resolved pixel size [154].

While still in its infancy, ULM has already provided a new *in-vivo* approach to the study of tissue pathology, providing quantitative information on the density, tortuosity, and small modulations of flow patterns within the microvasculature at depth. The first clinical applications of this technology, using conventional focused beam acquisition, have been conducted on breast cancer [155], lower limb assessment [156] and liver imaging [157]. While there are still limitations to this approach, including slow scan times, SNR, the use of plane-wave scanners not typical in clinics, large amounts of data storage and processing, and motion artefacts, significant advancements in all of these areas are currently ongoing.

4.5 Microbubble-Therapy Monitoring

It has long been recognized that ultrasound interactions with biological tissue induce bio-effects of both thermal and mechanical origin [158]. On clinical diagnostic scanners, exposure levels are limited in order to avoid these effects [159]. From a therapeutic standpoint, ultrasound-mediated bioeffects have been investigated as a desired endpoint: with effects ranging from tissue ablation [160], microvascular permeability [161], immunomodulation [162], and vascular occlusion [163]. Recent works have highlighted that microbubble contrast agents, under specific acoustic conditions, can generate a wide spectrum of bioeffects [164–166] that contribute towards the treatment of many diseases. Due to their intravascular nature, a primary avenue of research in microbubble-mediated bioeffects is based on the spatially targeted and temporary enhancement of microvascular permeability, employed to promote local drug delivery to regions of disease. One such promising application is the local and transient opening of the blood-brain-barrier [167, 168] and blood-spinal cord barrier [169, 170] for targeted therapeutics into the central nervous system. This technology has recently entered clinical trials in patients with brain tumors [171–173], Alzheimer's disease [174] and amyotrophic lateral sclerosis (ALS) [175].

Despite being met with initial success, widespread clinical adoption of microbubble-based therapeutics will require the continued development of online, real-time imaging strategies to

guide and control treatments. While some of these applications employ MRI guidance, there is increasing interest in employing the acoustic scattering from the microbubbles themselves as an indicator of treatment outcome. Since the spectral echo characteristics can be indicative of the underlying microbubble vibrations [176], remote detection of these signals during treatment is under investigation as a robust and sensitive tool for therapy guidance. Many preclinical applications of targeted microbubble therapeutics, including cardiovascular disease [177, 178] and cancer [166], are performed as a dual imaging and therapeutic technique. Contrast enhanced ultrasound is applied and interleaved with a therapeutic pulse from either a separate ultrasound transducer [166] or incorporated by way of clinical [179] or custom-designed sequence. In this way, the presence of microbubbles within the anatomical site of interest can be visually confirmed before, during and after the treatment sequences. The acoustic emissions detected during microbubble-based therapies have been identified as potential markers for treatment outcome in applications including blood-brain barrier disruption [180, 181], and targeted therapeutic delivery [182]. To this end, passive cavitation detectors are typically employed to measure raw acoustic data to extract quantitative metrics. Most of these methods to date utilize a single element passive transducer, which does not allow the bubble signal to be localized in space. Ongoing novel engineering of array transducers, combined with passive beamforming algorithms, are currently being designed to spatially map bubble activity and allow for confirmation that elicited bioeffects are localized to the target site [183, 184], see **Figure 5**. Above and beyond these correlative measures, efforts are underway to establish control feedback algorithms based on the measured bubble acoustic activity to promote safe levels of vibration and avoid more violent, disruptive bubble behaviour that leads to unwanted damage. These algorithms modulate the acoustic transmit parameters based off the real-time feedback from nonlinear microbubble emissions, including sub-harmonic energy [185, 186], harmonic energy [187, 188], or both [189].

5 CONCLUSION

Ultrasound contrast imaging using microbubbles is a safe and reliable technique for many clinical practices, and its application base is expanding. The tremendous success of this imaging technology to date is courtesy of increased clinical awareness of the benefits of ultrasound, and the collaborative research endeavors between physicists, chemists, engineers, and clinicians on the investigation of microbubble behavior, signal processing techniques, contrast agent synthesis, and device development. In this review, we summarized the fundamentals of contrast agent microbubble vibration and how it is harnessed for routine contrast-imaging application. Specific pulse sequences are employed to extract bubble-specific acoustic signatures and suppress signal arising from the surrounding tissue to enable preferential imaging of the vasculature. We then presented an overview of emerging techniques and technologies associated with microbubble-based imaging, summarized in **Table 2**. These developments span new design efforts on acoustically-sensitive agents for disease-specific imaging, to new signal processing techniques to obtain highly resolved vascular images, to new interpretation techniques to extract biologically/physiologically relevant data from microbubble acoustic signatures. With the development of new ultrafast imaging technology and image processing techniques, along with increasing interest in targeted ultrasound therapeutic applications, there are still numerous emerging and exciting applications that remain to be explored.

AUTHOR CONTRIBUTIONS

HY and BH co-led the scientific discussion and writing for this paper. BH is the corresponding author.

FUNDING

This work is supported, in part, by the NSERC (RGPIN-2019-06969), the Fonds de recherche du Quebec—Nature et Technologies (2021-NC-282699), the Heart and Stroke Foundation of Canada (G-18-0022133), the Canada Research Chair program, and the Burroughs Wellcome Fund (1018212.03). BH holds a Career at the Scientific Interface award from the Burroughs Wellcome Fund (BWF-CASI).

REFERENCES

1. Szabo TL. *Diagnostic Ultrasound Imaging: Inside and Out*. 1st ed. London, UK: Elsevier (2004).
2. Cobbold RSC, Chapter 5: Scattering of Ultrasound. In *Fundamentals of Biomedical Ultrasound* New York: Oxford University Press (2006). 268–329.
3. Jensen JA. *Estimation of Blood Velocities Using Ultrasound: A Signal Processing Approach*. New York: Cambridge University Press (1996).
4. Mone F, McAuliffe FM, Ong S. The Clinical Application of Doppler Ultrasound in Obstetrics. *Obstet Gynecol* (2015) 17(4):13–9. doi:10.1111/tog.12152
5. Grant EG, Benson CB, Moneta GL, Alexandrov AV, Baker JD, Bluth EI, et al. Carotid Artery Stenosis: Gray-Scale and Doppler US Diagnosis-Society of Radiologists in Ultrasound Consensus Conference. *Radiology* (2003) 229(2): 340–6. doi:10.1148/radiol.2292030516
6. Quiñones MA, Otto CM, Stoddard M, Waggoner A, Zoghbi WA. Recommendations for Quantification of Doppler Echocardiography: a Report from the Doppler Quantification Task Force of the Nomenclature and Standards Committee of the American Society of Echocardiography. *J Am Soc Echocardiography* (2002) 15(2):167–84. doi:10.1067/mje.2002.120202
7. RSC Cobbold. *Foundations of Biomedical Ultrasound*. New York: Oxford University Press (2006).
8. Becher H, Burns P. *Handbook of Contrast Echocardiography: Left Ventricular Function and Myocardial Perfusion*. Frankfurt: Springer-Verlag (2000).
9. Medwin H. Counting Bubbles Acoustically: a Review. *Ultrasonics* 15 (1977). p. 7–13. doi:10.1016/0041-624x(77)90005-1
10. Unger EC, Porter T, Culp W, Labell R, Matsunaga T, Zutshi R. Therapeutic Applications of Lipid-Coated Microbubbles. *Adv Drug Deliv Rev* (2004) 56(9):1291–314. doi:10.1016/j.addr.2003.12.006
11. Garg S, Thomas AA, Borden MA. The Effect of Lipid Monolayer In-Plane Rigidity on *In Vivo* Microbubble Circulation Persistence. *Biomaterials* (2013) 34(28):6862–70. doi:10.1016/j.biomaterials.2013.05.053
12. Wilson SR, Burns PN. Microbubble-enhanced US in Body Imaging: What Role. *Radiology* (2010) 257(1):24–39. doi:10.1148/radiol.10091210

13. Muskula PR, Main ML. Safety with Echocardiographic Contrast Agents. *Circ Cardiovasc Imaging* (2017) 10(4):1–9. doi:10.1161/CIRCIMAGING.116.005459
14. Kaufman DW. Risk of Anaphylaxis in a Hospital Population in Relation to the Use of Various Drugs: An International Study. *Pharmacoepidem Drug Safe* (2003) 12(3):195–202. doi:10.1002/pds.822
15. Beckett KR, Moriarity AK, Langer JM. Safe Use of Contrast media: What the Radiologist Needs to Know. *Radiographics* (2015) 35(6):1738–50. doi:10.1148/rg.2015150033
16. Fraum TJ, Ludwig DR, Bashir MR, Fowler KJ. Gadolinium-based Contrast Agents: A Comprehensive Risk Assessment. *J Magn Reson Imaging* (2017) 46(2):338–53. doi:10.1002/jmri.25625
17. McDonald JS, Hunt CH, Kolbe AB, Schmitz JJ, Hartman RP, Maddox DE, et al. Acute Adverse Events Following Gadolinium-Based Contrast Agent Administration: A Single-center Retrospective Study of 281 945 Injections. *Radiology* (2019) 292(3):620–7. doi:10.1148/radiol.2019182834
18. Burns PN. Imaging Microbubbles in Children: A Light Foot on the Gas. *J Ultrasound Med* (2021) 40(–2):2535–6. doi:10.1002/jum.15656
19. Porter TR, Xie F. Myocardial Perfusion Imaging with Contrast Ultrasound. *JACC: Cardiovasc Imaging* (2010) 3(2):176–87. doi:10.1016/j.jcmg.2009.09.024
20. Williams R. Dynamic Microbubble Contrast- Enhanced US to Measure Tumor Response to Targeted Therapy : A Proposed Clinical Protocol with Results from Renal Cell Carcinoma Patients Receiving Antiangiogenic Therapy. *Radiology* (2011) 260:581. doi:10.1148/radiol.11101893/-/DC1
21. Macioch JE, Katsamakis CD, Robin J, Liebson PR, Meyer PM, Geohas C, et al. Effect of Contrast Enhancement on Measurement of Carotid Artery Intimal Medial Thickness. *Vasc Med* (2004) 9(1):7–12. doi:10.1191/1358863x04vm522oa
22. Feinstein SB. Contrast Ultrasound Imaging of the Carotid Artery Vasa Vasorum and Atherosclerotic Plaque Neovascularization. *J Am Coll Cardiol* (2006) 48(2):236–43. doi:10.1016/j.jacc.2006.02.068
23. Burns PN, Wilson SR, Simpson DH. Pulse Inversion Imaging of Liver Blood Flow. *Invest Radiol* (2000) 35(1):58–71. doi:10.1097/00004424-200001000-00007
24. Wei K, Le E, Bin JP, Coggins M, Thorpe J, Kaul S. Quantification of Renal Blood Flow with Contrast-Enhanced Ultrasound. *J Am Coll Cardiol* (2001) 37(4):1135–40. doi:10.1016/s0735-1097(00)01210-9
25. Sridharan A, Eisenbrey JR, Dave JK, Forsberg F. Quantitative Nonlinear Contrast-Enhanced Ultrasound of the Breast. *Am J Roentgenology* (2016) 207(2):274–81. doi:10.2214/AJR.16.16315
26. Robotti D, Cammarota T, Debani P, Sarno A, Astegiano M. Activity of Crohn Disease: Value of Color-Power-Doppler and Contrast-Enhanced Ultrasonography. *Abdom Imaging* (2004) 29(6):648–52. doi:10.1007/s00261-003-0157-0
27. Jayaram TJV, Lynch M, Soutter WP, Cosgrove DO, Harvey CJ, Patel N. Ovarian Cancer Detected Non-invasively by Contrast-Enhanced Power Doppler Ultrasound. *BJOG: Intern J Obs Gyn* (2004) 111(6):619–22. doi:10.1111/j.1471-0528.2004.00157.x
28. Halpern EJ. Contrast-enhanced Ultrasound Imaging of Prostate Cancer. *Rev Urol* (2006) 8 Suppl 1(Suppl. 1):S29–37. Available: http://www.ncbi.nlm.nih.gov/pubmed/17021624%0Ahttp://www.pubmedcentral.nih.gov/articlerender.fcgi?artid=PMC1578528. (Accessed December 1, 2021)
29. Bartolotta TV, Midiri M, Galia M, Runza G, Attard M, Savoia G, et al. Qualitative and Quantitative Evaluation of Solitary Thyroid Nodules with Contrast-Enhanced Ultrasound: Initial Results. *Eur Radiol* (2006) 16(10):2234–41. doi:10.1007/s00330-006-0229-y
30. Doinikov AA, Bouakaz A. Review of Shell Models for Contrast Agent Microbubbles. *IEEE Trans Ultrason Ferroelect., Freq Contr* (2011) 58(5):981–93. doi:10.1109/TUFFC.2011.1899
31. Leighton TG. What Is Ultrasound. *Prog Biophys Mol Biol* (2007) 93(1–3):3–83. doi:10.1016/j.pbiomolbio.2006.07.026
32. Flynn HG. Cavitation Dynamics: II. Free Pulsations and Models for Cavitation Bubbles. *The J Acoust Soc America* (1975) 58(6):1160–70. doi:10.1121/1.380799
33. Apfel RE, Holland CK. Gauging the Likelihood of Cavitation from Short-Pulse, Low-Duty Cycle Diagnostic Ultrasound. *Ultrasound Med Biol* (1991) 17(2):179–85. doi:10.1016/0301-5629(91)90125-G
34. Mulvagh SL, Rakowski H, Vannan MA, Abdelmoneim SS, Becher H, Bierig SM, et al. American Society of Echocardiography Consensus Statement on the Clinical Applications of Ultrasonic Contrast Agents in Echocardiography. *J Am Soc Echocardiography* (2008) 21(11):1179–201. doi:10.1016/j.echo.2008.09.009
35. Lee JY, Minami Y, Choi BI, Lee WJ, Chou Y-H, Jeong WK, et al. The Afsumb Consensus Statements and Recommendations for the Clinical Practice of Contrast-Enhanced Ultrasound Using Sonazoid. *Ultrasonography* (2020) 39(3):191–220. doi:10.14366/usg.20057
36. Dietrich CF, Nolsøe CP, Barr RG, Berzigotti A, Burns PN, Cantisani V, et al. Guidelines and Good Clinical Practice Recommendations for Contrast Enhanced Ultrasound (CEUS) in the Liver - Update 2020 - WFUMB in Cooperation with EFSUMB, AFSUMB, AIUM, and FLAUS. *Ultraschall Med* (2020) 41(5):562–85. doi:10.1055/a-1177-0530
37. Hudson JM, Karshafian R, Burns PN. Quantification of Flow Using Ultrasound and Microbubbles: a Disruption Replenishment Model Based on Physical Principles. *Ultrasound Med Biol* (2009) 35(12):2007–20. doi:10.1016/j.ultrasmedbio.2009.06.1102
38. Wei K, Jayaweera AR, Firoozan S, Linka A, Skyba DM, Kaul S. Quantification of Myocardial Blood Flow with Ultrasound-Induced Destruction of Microbubbles Administered as a Constant Venous Infusion. *Circulation* (1998) 97(5):473–83. doi:10.1161/01.CIR.97.5.473
39. Chomas JE, Dayton P, May D, Ferrara K. Threshold of Fragmentation for Ultrasonic Contrast Agents. *J Biomed Opt* (2001) 6(2):141–50. doi:10.1117/1.1352752
40. Chen W-S, Matula TJ, Brayman AA, Crum LA. A Comparison of the Fragmentation Thresholds and Inertial Cavitation Doses of Different Ultrasound Contrast Agents. *J Acoust Soc America* (2003) 113(1):643–51. doi:10.1121/1.1529667
41. Sassaroli E, Hynynen K. Cavitation Threshold of Microbubbles in Gel Tunnels by Focused Ultrasound. *Ultrasound Med Biol* (2007) 33(10):1651–60. doi:10.1016/j.ultrasmedbio.2007.04.018
42. Helfield B, Black JJ, Qin B, Pacella J, Chen X, Villanueva FS. Fluid Viscosity Affects the Fragmentation and Inertial Cavitation Threshold of Lipid-Encapsulated Microbubbles. *Ultrasound Med Biol* (2016) 42(3):782–94. doi:10.1016/j.ultrasmedbio.2015.10.023
43. King DA, Malloy MJ, Roberts AC, Haak A, Yoder CC, O'Brien WD. Determination of Postexcitation Thresholds for Single Ultrasound Contrast Agent Microbubbles Using Double Passive Cavitation Detection. *J Acoust Soc America* (2010) 127(6):3449–55. doi:10.1121/1.3373405
44. Overvelde M, Garbin V, Sijl J, Dollet B, de Jong N, Lohse D, et al. Nonlinear Shell Behavior of Phospholipid-Coated Microbubbles. *Ultrasound Med Biol* (2010) 36(12):2080–92. doi:10.1016/j.ultrasmedbio.2010.08.015
45. Helfield BL, Goertz DE. Nonlinear Resonance Behavior and Linear Shell Estimates for Definity and MicroMarker Assessed with Acoustic Microbubble Spectroscopy. *J Acoust Soc America* (2013) 133(2):1158–68. doi:10.1121/1.4774379
46. Lauterborn W. Numerical Investigation of Nonlinear Oscillations of Gas Bubbles in Liquids. *J Acoust Soc America* (1976) 59:283–93. doi:10.1121/1.380884
47. Sijl J, Overvelde M, Dollet B, Garbin V, de Jong N, Lohse D, et al. "Compression-only" Behavior: A Second-Order Nonlinear Response of Ultrasound Contrast Agent Microbubbles. *J Acoust Soc America* (2011) 129(4):1729–39. doi:10.1121/1.3505116
48. de Jong N, Emmer M, Chin CT, Bouakaz A, Mastik F, Lohse D, et al. "Compression-Only" Behavior of Phospholipid-Coated Contrast Bubbles. *Ultrasound Med Biol* (2007) 33(4):653–6. doi:10.1016/j.ultrasmedbio.2006.09.016
49. Doinikov AA, Haac JF, Dayton PA. Resonance Frequencies of Lipid-Shelled Microbubbles in the Regime of Nonlinear Oscillations. *Ultrasonics* (2009) 49(2):263–8. doi:10.1016/j.ultras.2008.09.006
50. Stride E, Saffari N. Investigating the Significance of Multiple Scattering in Ultrasound Contrast Agent Particle Populations. *IEEE Trans Ultrason Ferroelect., Freq Contr* (2005) 52(12):2332–45. doi:10.1109/TUFFC.2005.1563278
51. Helfield BL, Leung BYC, Goertz DE. The Influence of Compliant Boundary Proximity on the Fundamental and Subharmonic Emissions from Individual Microbubbles. *J Acoust Soc America* (2014) 136(1):EL40–EL46. doi:10.1121/1.4885544

52. Brock-Fisher GA, Poland MD, Rafter PG. *Means for Increasing Sensitivity in Non-linear Ultrasound Imaging Systems.* " US5577505 A (1996).
53. Phillips PJ. Contrast Pulse Sequences (CPS): Imaging Nonlinear Microbubbles. *Proc IEEE Ultrason Symp* (2001) 2:1739–45. doi:10.1109/ultsym.2001.992057
54. Averkiou MA, Bruce MF, Powers JE, Sheeran PS, Burns PN. Imaging Methods for Ultrasound Contrast Agents. *Ultrasound Med Biol* (2020) 46(3):498–517. doi:10.1016/j.ultrasmedbio.2019.11.004
55. Tremblay-Darveau C, Sheeran PS, Vu CK, Williams R, Zhang Z, Bruce M, et al. The Role of Microbubble Echo Phase Lag in Multipulse Contrast-Enhanced Ultrasound Imaging. *IEEE Trans Ultrason Ferroelect., Freq Contr* (2018) 65(8):1389–401. doi:10.1109/TUFFC.2018.2841848
56. Lindner JR. Microbubbles in Medical Imaging: Current Applications and Future Directions. *Nat Rev Drug Discov* (2004) 3(6):527–33. doi:10.1038/nrd1417
57. Langeveld SAG, Meijlink B, Kooiman K. Phospholipid-coated Targeted Microbubbles for Ultrasound Molecular Imaging and Therapy. *Curr Opin Chem Biol* (2021) 63:171–9. doi:10.1016/j.cbpa.2021.04.013
58. Kaufmann BA, Sanders JM, Davis C, Xie A, Aldred P, Sarembock IJ, et al. Molecular Imaging of Inflammation in Atherosclerosis with Targeted Ultrasound Detection of Vascular Cell Adhesion Molecule-1. *Circulation* (2007) 116(3):276–84. doi:10.1161/CIRCULATIONAHA.106.684738
59. Willmann JK, Kimura RH, Deshpande N, Lutz AM, Cochran JR, Gambhir SS. Targeted Contrast-Enhanced Ultrasound Imaging of Tumor Angiogenesis with Contrast Microbubbles Conjugated to Integrin-Binding Knottin Peptides. *J Nucl Med* (2010) 51(3):433–40. doi:10.2967/jnumed.109.068007
60. Hamilton AJ, Huang S-L, Warnick D, Rabbat M, Kane B, Nagaraj A, et al. Intravascular Ultrasound Molecular Imaging of Atheroma Components *In Vivo*. *J Am Coll Cardiol* (2004) 43(3):453–60. doi:10.1016/j.jacc.2003.07.048
61. Weller GER, Lu E, Csikari MM, Klibanov AL, Fischer D, Wagner WR, et al. Ultrasound Imaging of Acute Cardiac Transplant Rejection with Microbubbles Targeted to Intercellular Adhesion Molecule-1. *Circulation* (2003) 108(2):218–24. doi:10.1161/01.CIR.0000080287.74762.60
62. Ellegala DB, Leong-Poi H, Carpenter JE, Klibanov AL, Kaul S, Shaffrey ME, et al. Imaging Tumor Angiogenesis with Contrast Ultrasound and Microbubbles Targeted to α V β 3. *Circulation* (2003) 108(3):336–41. doi:10.1161/01.CIR.0000080326.15367.0C
63. Bettinger T, Bussat P, Tardy I, Pochon S, Hyvelin J-M, Emmel P, et al. Ultrasound Molecular Imaging Contrast Agent Binding to Both E- and P-Selectin in Different Species. *Invest Radiol* (2012) 47(9):516–23. doi:10.1097/RLI.0b013e31825cc605
64. Willmann JK, Bonomo L, Testa AC, Rinaldi P, Rindi G, Valluru KS, et al. Ultrasound Molecular Imaging with BR55 in Patients with Breast and Ovarian Lesions: First-In-Human Results. *Jco* (2017) 35(19):2133–40. doi:10.1200/JCO.2016.70.8594
65. Smeenge M, Tranquart F, Mannaerts CK, de Reijke TM, van de Vijver MJ, Laguna MP, et al. First-in-Human Ultrasound Molecular Imaging with a VEGFR2-specific Ultrasound Molecular Contrast Agent (BR55) in Prostate Cancer. *Invest Radiol* (2017) 52(7):419–27. doi:10.1097/RLI.0000000000000362
66. Korpanty G, Carbon JG, Grayburn PA, Fleming JB, Brekken RA. Monitoring Response to Anticancer Therapy by Targeting Microbubbles to Tumor Vasculature. *Clin Cancer Res* (2007) 13(1):323–30. doi:10.1158/1078-0432.CCR-06-1313
67. Zhao S, Kruse DE, Ferrara KW, Dayton PA. Selective Imaging of Adherent Targeted Ultrasound Contrast Agents. *Phys Med Biol* (2007) 52(8):2055–72. doi:10.1088/0031-9155/52/8/002
68. Helfield BL, Cherin E, Foster FS, Goertz DE. The Effect of Binding on the Subharmonic Emissions from Individual Lipid-Encapsulated Microbubbles at Transmit Frequencies of 11 and 25 MHz. *Ultrasound Med Biol* (2013) 39(2):345–59. doi:10.1016/j.ultrasmedbio.2012.09.011
69. Inaba Y, Lindner JR. Molecular Imaging of Disease with Targeted Contrast Ultrasound Imaging. *Translational Res* (2012) 159(3):140–8. doi:10.1016/j.trsl.2011.12.001
70. Needles A, Couture O, Foster FS. A Method for Differentiating Targeted Microbubbles in Real Time Using Subharmonic Micro-ultrasound and Interframe Filtering. *Ultrasound Med Biol* (2009) 35(9):1564–73. doi:10.1016/j.ultrasmedbio.2009.04.006
71. Wang S, Wang CY, Unnikrishnan S, Klibanov AL, Hossack JA, Mauldin FW. Optical Verification of Microbubble Response to Acoustic Radiation Force in Large Vessels with *In Vivo* Results. *Invest Radiol* (2015) 50(11):772–84. doi:10.1097/RLI.0000000000000185
72. Dayton PA, Morgan KE, Klibanov AL, Brandenburger G, Nightingale KR, Ferrara KW. A Preliminary Evaluation of the Effects of Primary and Secondary Radiation Forces on Acoustic Contrast Agents. *IEEE Trans Ultrason Ferroelect., Freq Contr* (1997) 44(6):1264–77. doi:10.1109/58.656630
73. Dayton P, Klibanov A, Brandenburger G, Ferrara K. Acoustic Radiation Force *In Vivo*: a Mechanism to Assist Targeting of Microbubbles. *Ultrasound Med Biol* (1999) 25(8):1195–201. doi:10.1016/s0301-5629(99)00062-9
74. Zhao S, Borden M, Bloch SH, Kruse D, Ferrara KW, Dayton PA. Radiation-force Assisted Targeting Facilitates Ultrasonic Molecular Imaging. *Mol Imaging* (2004) 3(3):135–48. doi:10.1162/1535350042380317
75. Helfield B. A Review of Phospholipid Encapsulated Ultrasound Contrast Agent Microbubble Physics. *Ultrasound Med Biol* (2019) 45(2):282–300. doi:10.1016/j.ultrasmedbio.2018.09.020
76. Hasegawa T, Yosioka K. Acoustic-Radiation Force on a Solid Elastic Sphere. *J Acoust Soc America* (1969) 46(5B):1139–43. doi:10.1121/1.1911832
77. Crum LA. Bjerknes Forces on Bubbles in a Stationary Sound Field. *J Acoust Soc America* (1975) 57(6):1363–70. doi:10.1121/1.380614
78. Rychak JJ, Klibanov AL, Ley KF, Hossack JA. Enhanced Targeting of Ultrasound Contrast Agents Using Acoustic Radiation Force. *Ultrasound Med Biol* (2007) 33(7):1132–9. doi:10.1016/j.ultrasmedbio.2007.01.005
79. Frinking PJA, Tardy I, Théraulaz M, Arditi M, Powers J, Pochon S, et al. Effects of Acoustic Radiation Force on the Binding Efficiency of BR55, a VEGFR2-specific Ultrasound Contrast Agent. *Ultrasound Med Biol* (2012) 38(8):1460–9. doi:10.1016/j.ultrasmedbio.2012.03.018
80. Wang S, Mauldin FW, Klibanov AL, Hossack JA. Ultrasound-Based Measurement of Molecular Marker Concentration in Large Blood Vessels: A Feasibility Study. *Ultrasound Med Biol* (2015) 41(1):222–34. doi:10.1016/j.ultrasmedbio.2014.07.001
81. Abou-Elkacem L, Bachawal SV, Willmann JK. Ultrasound Molecular Imaging: Moving toward Clinical Translation. *Eur J Radiol* (2015) 84(9):1685–93. doi:10.1016/j.ejrad.2015.03.016
82. Matsumura Y, Maeda H. A New Concept for Macromolecular Therapeutics in Cancer Chemotherapy: Mechanism of Tumoritropic Accumulation of Proteins and the Antitumor Agent Smancs. *Cancer Res* (1986) 46(8):6387–92.
83. A.Dayton PP, Dayton PA. Phase-change Contrast Agents for Imaging and Therapy. *Cpd* (2012) 18(15):2152–65. doi:10.2174/138161212800099883
84. Helfield B, Zou Y, Matsuura N. Acoustically-Stimulated Nanobubbles: Opportunities in Medical Ultrasound Imaging and Therapy. *Front Phys* (2021) 9(May):1–14. doi:10.3389/fphy.2021.654374
85. Shapiro MG, Goodwill PW, Neogy A, Yin M, Foster FS, Schaffer DV, et al. Biogenic Gas Nanostructures as Ultrasonic Molecular Reporters. *Nat Nanotech* (2014) 9(4):311–6. doi:10.1038/nnano.2014.32
86. Kopechek JA, Haworth KJ, Raymond JL, Douglas Mast T, Perrin SR, Klegerman ME, et al. Acoustic Characterization of Echogenic Liposomes: Frequency-dependent Attenuation and Backscatter. *J Acoust Soc America* (2011) 130(5):3472–81. doi:10.1121/1.3626124
87. Kwan JJ, Myers R, Coviello CM, Graham SM, Shah AR, Stride E, et al. Ultrasound-Propelled Nanocups for Drug Delivery. *Small* (2015) 11(39):5305–14. doi:10.1002/smll.201501322
88. Sheeran PS, Yoo K, Williams R, Yin M, Foster FS, Burns PN. More Than Bubbles: Creating Phase-Shift Droplets from Commercially Available Ultrasound Contrast Agents. *Ultrasound Med Biol* (2017) 43(2):531–40. doi:10.1016/j.ultrasmedbio.2016.09.003
89. Choudhury SA, Xie F, Kutty S, Lof J, Stolze E, Porter TR. Selective Infarct Zone Imaging with Intravenous Acoustically Activated Droplets. *PLoS One* (2018) 13(12):e0207486–15. doi:10.1371/journal.pone.0207486
90. Sheeran PS, Wong VP, Luois S, McFarland RJ, Ross WD, Feingold S, et al. Decafluorobutane as a Phase-Change Contrast Agent for Low-Energy Extravascular Ultrasonic Imaging. *Ultrasound Med Biol* (2011) 37(9):1518–30. doi:10.1016/j.ultrasmedbio.2011.05.021
91. Schad KC, Hynynen K. In Vitrocharacterization of Perfluorocarbon Droplets for Focused Ultrasound Therapy. *Phys Med Biol* (2010) 55(17):4933–47. doi:10.1088/0031-9155/55/17/004

92. Kripfgans OD, Fowlkes JB, Miller DL, Eldevik OP, Carson PL. Acoustic Droplet Vaporization for Therapeutic and Diagnostic Applications. *Ultrasound Med Biol* (2000) 26(7):1177–89. doi:10.1016/S0301-5629(00)00262-3
93. Shpak O, Verweij M, Vos HJ, de Jong N, Lohse D, Versluis M. Acoustic Droplet Vaporization Is Initiated by Superharmonic Focusing. *Proc Natl Acad Sci USA* (2014) 111(5):1697–702. doi:10.1073/pnas.1312171111
94. Helfield BL, Yoo K, Liu J, Williams R, Sheeran PS, Goertz DE, et al. Investigating the Accumulation of Submicron Phase-Change Droplets in Tumors. *Ultrasound Med Biol* (2020) 46(10):2861–70. doi:10.1016/j.ultrasmedbio.2020.06.021
95. Williams R, Wright C, Cherin E, Reznik N, Lee M, Gorelikov I, et al. Characterization of Submicron Phase-Change Perfluorocarbon Droplets for Extravascular Ultrasound Imaging of Cancer. *Ultrasound Med Biol* (2013) 39(3):475–89. doi:10.1016/j.ultrasmedbio.2012.10.004
96. Exner AA, Kolios MC. Bursting Microbubbles: How Nanobubble Contrast Agents Can Enable the Future of Medical Ultrasound Molecular Imaging and Image-Guided Therapy. *Curr Opin Colloid Interf Sci* (2021) 54:101463. doi:10.1016/j.cocis.2021.101463
97. Perera RH, Wu H, Peiris P, Hernandez C, Burke A, Zhang H, et al. Improving Performance of Nanoscale Ultrasound Contrast Agents Using N,N-diethylacrylamide Stabilization. *Nanomedicine: Nanotechnology, Biol Med* (2017) 13(1):59–67. doi:10.1016/j.nano.2016.08.020
98. Pellow C, Acconcia C, Zheng G, Goertz DE. Threshold-dependent Nonlinear Scattering from Porphyrin Nanobubbles for Vascular and Extravascular Applications. *Phys Med Biol* (2018) 63:215001–21. doi:10.1088/1361-6560/aae571
99. Pellow C, Tan J, Chérin E, Demore CEM, Zheng G, Goertz DE. High Frequency Ultrasound Nonlinear Scattering from Porphyrin Nanobubbles. *Ultrasonics* (2021) 110:106245. doi:10.1016/j.ultras.2020.106245
100. Pellow C, Abenojar EC, Exner AA, Zheng G, Goertz DE. Concurrent Visual and Acoustic Tracking of Passive and Active Delivery of Nanobubbles to Tumors. *Theranostics* (2020) 10(25):11690–706. doi:10.7150/thno.51316
101. Pellow C, O'Reilly MA, Hynynen K, Zheng G, Goertz DE. Simultaneous Intravital Optical and Acoustic Monitoring of Ultrasound-Triggered Nanobubble Generation and Extravasation. *Nano Lett* (2020) 20(6):4512–9. doi:10.1021/acs.nanolett.0c01310
102. Walsby AE Gas Vesicles. *Microbiol Rev* (1994) 58(1):94–144. doi:10.1128/mmbr.58.1.94-144.199410.1128/mr.58.1.94-144.1994
103. Maresca D, Lakshmanan A, Abedi M, Bar-Zion A, Farhadi A, Lu GJ, et al. Biomolecular Ultrasound and Sonogenetics. *Annu Rev Chem Biomol Eng* (2018) 9:229–52. doi:10.1146/annurev-chembioeng-060817-084034
104. Cherin E, Melis JM, Bourdeau RW, Yin M, Kochmann DM, Foster FS, et al. Acoustic Behavior of Halobacterium Salinarum Gas Vesicles in the High-Frequency Range: Experiments and Modeling. *Ultrasound Med Biol* (2017) 43(5):1016–30. doi:10.1016/j.ultrasmedbio.2016.12.020
105. Maresca D, Lakshmanan A, Lee-Gosselin A, Melis JM, Ni Y-L, Bourdeau RW, et al. Nonlinear Ultrasound Imaging of Nanoscale Acoustic Biomolecules. *Appl Phys Lett* (2017) 110(7):073704–5. doi:10.1063/1.4976105
106. Lakshmanan A, Farhadi A, Nety SP, Lee-Gosselin A, Bourdeau RW, Maresca D, et al. Molecular Engineering of Acoustic Protein Nanostructures. *ACS Nano* (2016) 10(8):7314–22. doi:10.1021/acsnano.6b03364
107. Lakshmanan A, Jin Z, Nety SP, Sawyer DP, Lee-Gosselin A, Malounda D, et al. Acoustic Biosensors for Ultrasound Imaging of Enzyme Activity. *Nat Chem Biol* (2020) 16(9):988–96. doi:10.1038/s41589-020-0591-0
108. Farhadi A, Ho GH, Sawyer DP, Bourdeau RW, Shapiro MG. Ultrasound Imaging of Gene Expression in Mammalian Cells. *Science* (2019) 365(6460):1469–75. doi:10.1126/science.aax4804
109. Bouakaz A, Frigstad S, Ten Cate FJ, de Jong N. Super Harmonic Imaging: A New Imaging Technique for Improved Contrast Detection. *Ultrasound Med Biol* (2002) 28(1):59–68. doi:10.1016/S0301-5629(01)00460-4
110. M. J. Van Neer PL, Matte G, Danilouchkine MG, Prins C, Van Den Adel F, De Jong N. Super-Harmonic Imaging: Development of an Interleaved Phased-Array Transducer. *IEEE Trans Ultrason Ferroelect., Freq Contr* (2010) 57(2):455–68. doi:10.1109/TUFFC.2010.1426
111. Kruse DE, Ferrara KW. A New Imaging Strategy Using Wideband Transient Response of Ultrasound Contrast Agents. *IEEE Trans Ultrason Ferroelect., Freq Contr* (2005) 52(8):1320–9. doi:10.1109/tuffc.2005.1509790
112. Guiroy A, Novell A, Ringgaard E, Lou-Moeller R, Gregoire J-m., Abellard A-p., et al. Dual-frequency Transducer for Nonlinear Contrast Agent Imaging. *IEEE Trans Ultrason Ferroelect., Freq Contr* (2013) 60(12):2634–44. doi:10.1109/TUFFC.2013.2862
113. Gessner R, Lukacs M, Lee M, Cherin E, Foster FS, Dayton PA. High-resolution, High-Contrast Ultrasound Imaging Using a Prototype Dual-Frequency Transducer: *In Vitro* and *In Vivo* Studies. *IEEE Trans Ultrason Ferroelect., Freq Contr* (2010) 57(8):1772–81. doi:10.1109/TUFFC.2010.1615
114. Lindsey B, Rojas J, Martin K, Shelton S, Dayton P. Acoustic Characterization of Contrast-To-Tissue Ratio and Axial Resolution for Dual-Frequency Contrast-specific Acoustic Angiography Imaging. *IEEE Trans Ultrason Ferroelect., Freq Contr* (2014) 61(10):1668–87. doi:10.1109/TUFFC.2014.006466
115. Newsome IG, Dayton PA. Visualization of Microvascular Angiogenesis Using Dual-Frequency Contrast-Enhanced Acoustic Angiography: A Review. *Ultrasound Med Biol* (2020) 46(10):2625–35. doi:10.1016/j.ultrasmedbio.2020.06.009
116. Lin F, Shelton SE, Espíndola D, Rojas JD, Pinton G, Dayton PA. 3-D Ultrasound Localization Microscopy for Identifying Microvascular Morphology Features of Tumor Angiogenesis at a Resolution beyond the Diffraction Limit of Conventional Ultrasound. *Theranostics* (2017) 7(1):196–204. doi:10.7150/thno.16899
117. Shelton SE, Lee YZ, Lee M, Cherin E, Foster FS, Aylward SR, et al. Quantification of Microvascular Tortuosity during Tumor Evolution Using Acoustic Angiography. *Ultrasound Med Biol* (2015) 41(7):1896–904. doi:10.1016/j.ultrasmedbio.2015.02.012
118. Yang J, Cherin E, Yin J, Newsome IG, Kierski TM, Pang G, et al. Characterization of an Array-Based Dual-Frequency Transducer for Superharmonic Contrast Imaging. *IEEE Trans Ultrason Ferroelect., Freq Contr* (2021) 68(7):2419–31. doi:10.1109/TUFFC.2021.3065952
119. Newsome IG, Kierski TM, Pang G, Yin J, Yang J, Cherin E, et al. Implementation of a Novel 288-Element Dual-Frequency Array for Acoustic Angiography: *In Vitro* and *In Vivo* Characterization. *IEEE Trans Ultrason Ferroelect., Freq Contr* (2021) 68(8):2657–66. doi:10.1109/TUFFC.2021.3074025
120. Bosch J, Groszmann RJ, Shah VH Evolution in the Understanding of the Pathophysiological Basis of portal Hypertension: How Changes in Paradigm Are Leading to Successful New Treatments. *J Hepatol* (2015) 62(S1):S121–S130. doi:10.1016/j.jhep.2015.01.003
121. Fairbank WM, Scully MO A New Noninvasive Technique for Cardiac Pressure Measurement: Resonant Scattering of Ultrasound from Bubbles. *IEEE Trans Biomed Eng* (1977) BME-24(2):107–10. doi:10.1109/TBME.1977.326112
122. Dave JK, Kulkarni SV, Pangaonkar PP, Stanczak M, McDonald ME, Cohen IS, et al. Non-Invasive Intra-cardiac Pressure Measurements Using Subharmonic-Aided Pressure Estimation: Proof of Concept in Humans. *Ultrasound Med Biol* (2017) 43(11):2718–24. doi:10.1016/j.ultrasmedbio.2017.07.009
123. Tremblay-Darveau C, Williams R, Burns PN Measuring Absolute Blood Pressure Using Microbubbles. *Ultrasound Med Biol* (2014) 40(4):775–87. doi:10.1016/j.ultrasmedbio.2013.10.017
124. Shankar PM, Krishna PD, Newhouse VL. Subharmonic Backscattering from Ultrasound Contrast Agents. *J Acoust Soc Am* (1999) 106(4 Pt 1):2104–10. doi:10.1121/1.428142
125. Forsberg F, Ji-Bin Liu J, Shi WT, Furuse J, Shimizu M, Goldberg BB *In Vivo* pressure Estimation Using Subharmonic Contrast Microbubble Signals: Proof of Concept. *IEEE Trans Ultrason Ferroelect., Freq Contr* (2005) 52(4):581–3. doi:10.1109/tuffc.2005.1428040
126. Dave JK, Halldorsdottir VG, Eisenbrey JR, Merton DA, Liu J-B, Zhou J-H, et al. Investigating the Efficacy of Subharmonic Aided Pressure Estimation for Portal Vein Pressures and Portal Hypertension Monitoring. *Ultrasound Med Biol* (2012) 38(10):1784–98. doi:10.1016/j.ultrasmedbio.2012.06.013
127. Halldorsdottir VG, Dave JK, Eisenbrey JR, Machado P, Zhao H, Liu JB, et al. Subharmonic Aided Pressure Estimation for Monitoring Interstitial Fluid Pressure in Tumours - *In Vitro* and *In Vivo* Proof of Concept. *Ultrasonics* (2014) 54(7):1938–44. doi:10.1016/j.ultras.2014.04.022
128. Eisenbrey JR, Dave JK, Halldorsdottir VG, Merton DA, Miller C, Gonzalez JM, et al. Chronic Liver Disease: Noninvasive Subharmonic Aided Pressure

Estimation of Hepatic Venous Pressure Gradient. *Radiology* (2013) 268(2): 581–8. doi:10.1148/radiol.13121769
129. Sandrin L, Catheline S, Tanter M, Hennequin X, Fink M Time-resolved Pulsed Elastography with Ultrafast Ultrasonic Imaging. *Ultrason Imaging* (1999) 21(4):259–72. doi:10.1177/016173469902100402
130. Maresca D, Correia M, Villemain O, Bizé A, Sambin L, Tanter M, et al. Noninvasive Imaging of the Coronary Vasculature Using Ultrafast Ultrasound. *JACC: Cardiovasc Imaging* (2018) 11(6):798–808. doi:10.1016/j.jcmg.2017.05.021
131. Tremblay-Darveau C, Williams R, Milot L, Bruce M, Burns PN Combined Perfusion and Doppler Imaging Using Plane-Wave Nonlinear Detection and Microbubble Contrast Agents. *IEEE Trans Ultrason Ferroelect., Freq Contr* (20002014) 61(12):1988–2000. doi:10.1109/TUFFC.2014.006573
132. Couture O, Besson B, Montaldo G, Fink M, Tanter M Microbubble Ultrasound Super-localization Imaging (MUSLI). *IEEE Int Ultrason Symp IUS* (2011) 1285–7. doi:10.1109/ULTSYM.2011.6293576
133. Lowerison MR, Huang C, Lucien F, Chen S, Song P Ultrasound Localization Microscopy of Renal Tumor Xenografts in Chicken Embryo Is Correlated to Hypoxia. *Sci Rep* (2020) 10(1):1–13. doi:10.1038/s41598-020-59338-z
134. O'Reilly MA, Hynynen K A Super-resolution Ultrasound Method for Brain Vascular Mapping. *Med Phys* (2013) 40(11):110701–7. doi:10.1118/1.4823762
135. Errico C, Pierre J, Pezet S, Desailly Y, Lenkei Z, Couture O, et al. Ultrafast Ultrasound Localization Microscopy for Deep Super-resolution Vascular Imaging. *Nature* (2015) 527(7579):499–502. doi:10.1038/nature16066
136. Christensen-Jeffries K, Couture O, Dayton PA, Eldar YC, Hynynen K, Kiessling F, et al. Super-resolution Ultrasound Imaging. *Ultrasound Med Biol* (2020) 46(4):865–91. doi:10.1016/j.ultrasmedbio.2019.11.013
137. Couture O, Hingot V, Heiles B, Muleki-Seya P, Tanter M Ultrasound Localization Microscopy and Super-resolution: A State of the Art. *IEEE Trans Ultrason Ferroelect., Freq Contr* (2018) 65(8):1304–20. doi:10.1109/TUFFC.2018.2850811
138. Betzig E, Patterson GH, Sougrat R, Lindwasser OW, Olenych S, Bonifacino JS, et al. Imaging Intracellular Fluorescent Proteins at Nanometer Resolution. *Science* (2006) 313(5793):1642–5. doi:10.1126/science.1127344
139. Rust MJ, Bates M, Zhuang X Sub-diffraction-limit Imaging by Stochastic Optical Reconstruction Microscopy (STORM). *Nat Methods* (2006) 3(10): 793–6. doi:10.1038/nmeth929
140. Hess ST, Girirajan TPK, Mason MD Ultra-high Resolution Imaging by Fluorescence Photoactivation Localization Microscopy. *Biophysical J* (2006) 91(11):4258–72. doi:10.1529/biophysj.106.091116
141. Viessmann OM, Eckersley RJ, Christensen-Jeffries K, Tang MX, Dunsby C Acoustic Super-resolution with Ultrasound and Microbubbles. *Phys Med Biol* (2013) 58(18):6447–58. doi:10.1088/0031-9155/58/18/6447
142. Siepmann M, Schmitz G, Bzyl J, Palmowski M, Kiessling F Imaging Tumor Vascularity by Tracing Single Microbubbles. *IEEE Int Ultrason Symp IUS* (2011) 1908. doi:10.1109/ULTSYM.2011.0476
143. Hingot V, Errico C, Tanter M, Couture O Subwavelength Motion-Correction for Ultrafast Ultrasound Localization Microscopy. *Ultrasonics* (2017) 77: 17–21. doi:10.1016/j.ultras.2017.01.008
144. Foiret J, Zhang H, Ilovitsh T, Mahakian L, Tam S, Ferrara KW Ultrasound Localization Microscopy to Image and Assess Microvasculature in a Rat Kidney. *Sci Rep* (2017) 7(1):1–12. doi:10.1038/s41598-017-13676-7
145. Song P, Trzasko JD, Manduca A, Huang R, Kadirvel R, Kallmes DF, et al. Improved Super-resolution Ultrasound Microvessel Imaging with Spatiotemporal Nonlocal Means Filtering and Bipartite Graph-Based Microbubble Tracking. *IEEE Trans Ultrason Ferroelect., Freq Contr* (2018) 65(2):149–67. doi:10.1109/ULTSYM.2017.8092824
146. Heiles B, Correia M, Hingot V, Pernot M, Provost J, Tanter M, et al. Ultrafast 3D Ultrasound Localization Microscopy Using a 32 $\times$ 32 Matrix Array. *IEEE Trans Med Imaging* (2019) 38(9):2005–15. doi:10.1109/TMI.2018.2890358
147. Desailly Y, Tissier A-M, Correas J-M, Wintzenrieth F, Tanter M, Couture O Contrast Enhanced Ultrasound by Real-Time Spatiotemporal Filtering of Ultrafast Images. *Phys Med Biol* (2017) 62(1):31–42. doi:10.1088/1361-6560/62/1/31
148. Christensen-Jeffries K, Brown J, Aljabar P, Tang M, Dunsby C, Eckersley RJ 3-D *In Vitro* Acoustic Super-resolution and Super-resolved Velocity Mapping Using Microbubbles. *IEEE Trans Ultrason Ferroelect., Freq Contr* (2017) 64(10):1478–86. doi:10.1109/TUFFC.2017.2731664
149. Christensen-Jeffries K, Harput S, Brown J, Wells PNT, Aljabar P, Dunsby C, et al. Microbubble Axial Localization Errors in Ultrasound Super-resolution Imaging. *IEEE Trans Ultrason Ferroelect., Freq Contr* (2017) 64(11):1644–54. doi:10.1109/ULTSYM.2017.809184610.1109/tuffc.2017.2741067
150. Huang C, Lowerison MR, Trzasko JD, Manduca A, Bresler Y, Tang S, et al. Short Acquisition Time Super-resolution Ultrasound Microvessel Imaging via Microbubble Separation. *Sci Rep* (2020) 10(1):1–13. doi:10.1038/s41598-020-62898-9
151. Soylu U, Bresler Y Circumventing the Resolution-Time Tradeoff in Ultrasound Localization Microscopy by Velocity Filtering (2021). 1–17. Available: http://arxiv.org/abs/2101.09470. (Accessed December 1, 2021)
152. Van Sloun RJG, Solomon O, Bruce M, Khaing ZZ, Wijkstra H, Eldar YC, et al. Super-Resolution Ultrasound Localization Microscopy through Deep Learning. *IEEE Trans Med Imaging* (2021) 40(3):829–39. doi:10.1109/TMI.2020.3037790
153. Ackermann D, Schmitz G Detection and Tracking of Multiple Microbubbles in Ultrasound B-Mode Images. *IEEE Trans Ultrason Ferroelect., Freq Contr* (2016) 63(1):72–82. doi:10.1109/TUFFC.2015.2500266
154. Hingot V, Errico C, Heiles B, Rahal L, Tanter M, Couture O Microvascular Flow Dictates the Compromise between Spatial Resolution and Acquisition Time in Ultrasound Localization Microscopy. *Sci Rep* (2019) 9(1):1–10. doi:10.1038/s41598-018-38349-x
155. Opacic T, Dencks S, Theek B, Piepenbrock M, Ackermann D, Rix A, et al. Motion Model Ultrasound Localization Microscopy for Preclinical and Clinical Multiparametric Tumor Characterization. *Nat Commun* (2018) 9(1):1–13. doi:10.1038/s41467-018-03973-8
156. Harput S, Christensen-Jeffries K, Brown J, Li Y, Williams KJ, Davies AH, et al. Two-Stage Motion Correction for Super-resolution Ultrasound Imaging in Human Lower Limb. *IEEE Trans Ultrason Ferroelect., Freq Contr* (2018) 65(5):803–14. doi:10.1109/TUFFC.2018.2824846
157. Huang C, Zhang W, Gong P, Lok U-W, Tang S, Yin T, et al. Super-resolution Ultrasound Localization Microscopy Based on a High Frame-Rate Clinical Ultrasound Scanner: An In-Human Feasibility Study. *Phys Med Biol* (2021) 66(8):08NT01. doi:10.1088/1361-6560/abef45
158. Wood RW, Loomis AL XXXVIII.The Physical and Biological Effects of High-Frequency Sound-Waves of Great Intensity. *Lond Edinb Dublin Phil Mag J Sci* (1927) 4(22):417–36. doi:10.1080/14786440908564348
159. Fowlkes JB. American Institute of Ultrasound in Medicine Consensus Report on Potential Bioeffects of Diagnostic Ultrasound: Executive Summary. *J Ultrasound Med* (2008) 27(4):503–15. doi:10.7863/jum.2008.27.4.503
160. ter Haar G, Coussios C High Intensity Focused Ultrasound: Physical Principles and Devices. *Int J Hyperthermia* (2007) 23(2):89–104. doi:10.1080/02656730601186138
161. Skyba DM, Price RJ, Linka AZ, Skalak TC, Kaul S Direct *In Vivo* Visualization of Intravascular Destruction of Microbubbles by Ultrasound and its Local Effects on Tissue. *Circulation* (1998) 98: 290–3. doi:10.1161/01.CIR.98.4.290
162. Blackmore J, Shrivastava S, Sallet J, Butler CR, Cleveland RO Ultrasound Neuromodulation: A Review of Results, Mechanisms and Safety. *Ultrasound Med Biol* (2019) 45(7):1509–36. doi:10.1016/j.ultrasmedbio.2018.12.015
163. Hynynen K, Colucci V, Chung A, Jolesz F Noninvasive Arterial Occlusion Using MRI-Guided Focused Ultrasound. *Ultrasound Med Biol* (1996) 22(8): 1071–7. doi:10.1016/s0301-5629(96)00143-3
164. Chen H, Kreider W, Brayman AA, Bailey MR, Matula TJ Blood Vessel Deformations on Microsecond Time Scales by Ultrasonic Cavitation. *Phys Rev Lett* (2011) 106(3):1–4. doi:10.1103/PhysRevLett.106.034301
165. Helfield B, Chen X, Watkins SC, Villanueva FS Biophysical Insight into Mechanisms of Sonoporation. *Proc Natl Acad Sci USA* (2016) 113(36): 9983–8. doi:10.1073/pnas.1606915113
166. Goertz DE, Todorova M, Mortazavi O, Agache V, Chen B, Karshafian R, et al. Antitumor Effects of Combining Docetaxel (Taxotere) with the Antivascular Action of Ultrasound Stimulated Microbubbles. *PLoS One* (2012) 7(12): e52307. doi:10.1371/journal.pone.0052307
167. Hynynen K, Mcdannold N, Vykhodtseva N, Jolesz FA Noninvasive MR Imaging-Guided Focal Opening of the Blood-Brain Barrier in Rabbits. *Radiology* (2001) 220(3):640–6. doi:10.1148/radiol.2202001804

168. Hynynen K, McDannold N, Sheikov NA, Jolesz FA, Vykhodtseva N Local and Reversible Blood-Brain Barrier Disruption by Noninvasive Focused Ultrasound at Frequencies Suitable for Trans-skull Sonications. *Neuroimage* (2005) 24(1):12–20. doi:10.1016/j.neuroimage.2004.06.046
169. Weber-Adrian D, Thévenot E, O'Reilly MA, Oakden W, Akens MK, Ellens N, et al. Gene Delivery to the Spinal Cord Using MRI-Guided Focused Ultrasound. *Gene Ther* (2015) 22(7):568–77. doi:10.1038/gt.2015.25
170. O'Reilly MA, Chinnery T, Yee M-L, Wu S-K, Hynynen K, Kerbel RS, et al. Preliminary Investigation of Focused Ultrasound-Facilitated Drug Delivery for the Treatment of Leptomeningeal Metastases. *Sci Rep* (2018) 8(1):1–8. doi:10.1038/s41598-018-27335-y
171. Mainprize T, Lipsman N, Huang Y, Meng Y, Bethune A, Ironside S, et al. Blood-Brain Barrier Opening in Primary Brain Tumors with Non-invasive MR-Guided Focused Ultrasound: A Clinical Safety and Feasibility Study. *Sci Rep* (2019) 9(1):1–7. doi:10.1038/s41598-018-36340-0
172. Carpentier A, Canney M, Vignot A, Reina V, Beccaria K, Horodyckid C, et al. Clinical Trial of Blood-Brain Barrier Disruption by Pulsed Ultrasound. *Sci Transl Med* (2016) 8(343):1–7. doi:10.1126/scitranslmed.aaf6086
173. Park SH, Kim MJ, Jung HH, Chang WS, Choi HS, Rachmilevitch I, et al. Safety and Feasibility of Multiple Blood-Brain Barrier Disruptions for the Treatment of Glioblastoma in Patients Undergoing Standard Adjuvant Chemotherapy. *J Neurosurg* (2021) 134(2):475–83. doi:10.3171/2019.10.JNS192206
174. Lipsman N, Meng Y, Bethune AJ, Huang Y, Lam B, Masellis M, et al. Blood-brain Barrier Opening in Alzheimer's Disease Using MR-Guided Focused Ultrasound. *Nat Commun* (2018) 9(1):2336. doi:10.1038/s41467-018-04529-6
175. Abrahao A, Meng Y, Llinas M, Huang Y, Hamani C, Mainprize T, et al. First-in-human Trial of Blood-Brain Barrier Opening in Amyotrophic Lateral Sclerosis Using MR-Guided Focused Ultrasound. *Nat Commun* (2019) 10(–9):1. doi:10.1038/s41467-019-12426-9
176. Sijl J, Vos HJ, Rozendal T, de Jong N, Lohse D, Versluis M Combined Optical and Acoustical Detection of Single Microbubble Dynamics. *J Acoust Soc America* (2011) 130(5):3271–81. doi:10.1121/1.3626155
177. Shohet RV, Chen S, Zhou Y-T, Wang Z, Meidell RS, Unger RH, et al. Echocardiographic Destruction of Albumin Microbubbles Directs Gene Delivery to the Myocardium. *Circulation* (2000) 101(22):2554–6. doi:10.1161/01.CIR.101.22.2554
178. Leong-Poi H, Kuliszewski MA, Lekas M, Sibbald M, Teichert-Kuliszewska K, Klibanov AL, et al. Therapeutic Arteriogenesis by Ultrasound-Mediated VEGF 165 Plasmid Gene Delivery to Chronically Ischemic Skeletal Muscle. *Circ Res* (2007) 101(3):295–303. doi:10.1161/CIRCRESAHA.107.148676
179. Mathias W, Tsutsui JM, Tavares BG, Xie F, Aguiar MOD, Garcia DR, et al. Diagnostic Ultrasound Impulses Improve Microvascular Flow in Patients with STEMI Receiving Intravenous Microbubbles. *J Am Coll Cardiol* (2016) 67(21):2506–15. doi:10.1016/j.jacc.2016.03.542
180. McDannold N, Vykhodtseva N, Hynynen K Targeted Disruption of the Blood-Brain Barrier with Focused Ultrasound: Association with Cavitation Activity. *Phys Med Biol* (2006) 51(4):793–807. doi:10.1088/0031-9155/51/4/003
181. Tung Y-S, Vlachos F, Choi JJ, Deffieux T, Selert K, Konofagou EE In Vivotranscranial Cavitation Threshold Detection during Ultrasound-Induced Blood-Brain Barrier Opening in Mice. *Phys Med Biol* (2010) 55(20):6141–55. doi:10.1088/0031-9155/55/20/007
182. Kopechek JA, Carson AR, McTiernan CF, Chen X, Klein EC, Villanueva FS Cardiac Gene Expression Knockdown Using Small Inhibitory RNA-Loaded Microbubbles and Ultrasound. *PLoS One* (2016) 11(7):e0159751–12. doi:10.1371/journal.pone.0159751
183. Jones RM, McMahon D, Hynynen K Ultrafast Three-Dimensional Microbubble Imaging *In Vivo* Predicts Tissue Damage Volume Distributions during Nonthermal Brain Ablation. *Theranostics* (2020) 10(16):7211–30. doi:10.7150/thno.47281
184. Choi JJ, Carlisle RC, Coviello C, Seymour L, Coussios C-C Non-invasive and Real-Time Passive Acoustic Mapping of Ultrasound-Mediated Drug Delivery. *Phys Med Biol* (2014) 59(17):4861–77. doi:10.1088/0031-9155/59/17/4861
185. O'Reilly MA, Hynynen K Real-time Feedback-Controlled Focused Ultrasound Disruption by Using an Acoustic Emissions – Based Controller. *Radiology* (2012) 263(1):96–106.
186. Bing C, Hong Y, Hernandez C, Rich M, Cheng B, Munaweera I, et al. Characterization of Different Bubble Formulations for Blood-Brain Barrier Opening Using a Focused Ultrasound System with Acoustic Feedback Control. *Sci Rep* (2018) 8(1):1–12. doi:10.1038/s41598-018-26330-7
187. Arvanitis CD, Livingstone MS, Vykhodtseva N, McDannold N Controlled Ultrasound-Induced Blood-Brain Barrier Disruption Using Passive Acoustic Emissions Monitoring. *PLoS One* (2012) 7(9):e45783. doi:10.1371/journal.pone.0045783
188. Sun T, Zhang Y, Power C, Alexander PM, Sutton JT, Aryal M, et al. Closed-loop Control of Targeted Ultrasound Drug Delivery across the Blood-Brain/tumor Barriers in a Rat Glioma Model. *Proc Natl Acad Sci USA* (2017) 114(48):E10281–E10290. doi:10.1073/pnas.1713328114
189. Kamimura HA, Flament J, Valette J, Cafarelli A, Aron Badin R, Hantraye P, et al. Feedback Control of Microbubble Cavitation for Ultrasound-Mediated Blood-Brain Barrier Disruption in Non-human Primates under Magnetic Resonance Guidance. *J Cereb Blood Flow Metab* (2019) 39(7):1191–203. doi:10.1177/0271678X17753514
190. Goertz DE, de Jong N, van der Steen AFW Attenuation and Size Distribution Measurements of Definity and Manipulated Definity Populations. *Ultrasound Med Biol* (2007) 33(9):1376–88. doi:10.1016/j.ultrasmedbio.2007.03.009
191. Helfield BL, Huo X, Williams R, Goertz DE The Effect of Preactivation Vial Temperature on the Acoustic Properties of DefinityTM. *Ultrasound Med Biol* (2012) 38(7):1298–305. doi:10.1016/j.ultrasmedbio.2012.03.005
192. Hyvelin J-M, Gaud E, Costa M, Helbert A, Bussat P, Bettinger T, et al. Characteristics and Echogenicity of Clinical Ultrasound Contrast Agents: An *In Vitro* and *In Vivo* Comparison Study. *J Ultrasound Med* (2017) 36(5):941–53. doi:10.7863/ultra.16.04059
193. Shekhar H, Smith NJ, Raymond JL, Holland CK, "Effect of Temperature on the Size Distribution, Shell Properties, and Stability of Definity," *Ultrasound Med Biol*, (2018), 44, 434–46. doi:10.1016/j.ultrasmedbio.2017.09.021
194. Stapleton S, Goodman H, Zhou Y-Q, Cherin E, Henkelman RM, Burns PN, et al. Acoustic and Kinetic Behaviour of Definity in Mice Exposed to High Frequency Ultrasound. *Ultrasound Med Biol* (2009) 35(2):296–307. doi:10.1016/j.ultrasmedbio.2008.08.010
195. Faez T, Goertz D, De Jong N Characterization of Definity Ultrasound Contrast Agent at Frequency Range of 5-15 MHz. *Ultrasound Med Biol* (2011) 37(2):338–42. doi:10.1016/j.ultrasmedbio.2010.11.014
196. Schneider M SonoVue, a New Ultrasound Contrast Agent. *Eur Radiol* (1999) 9(3 Suppl. L):S347–S348. doi:10.1007/pl00014071
197. Gorce J-M, Arditi M, Schneider M Influence of Bubble Size Distribution on the Echogenicity of Ultrasound Contrast Agents. *Invest Radiol* (2000) 35(11):661–71. doi:10.1097/00004424-200011000-00003
198. Shi WT, Forsberg F Ultrasonic Characterization of the Nonlinear Properties of Contrast Microbubbles. *Ultrasound Med Biol* (2000) 26(1):93–104. doi:10.1016/s0301-5629(99)00117-9
199. Sontum PC Physicochemical Characteristics of Sonazoid, a New Contrast Agent for Ultrasound Imaging. *Ultrasound Med Biol* (2008) 34(5):824–33. doi:10.1016/j.ultrasmedbio.2007.11.006
200. Sarkar K, Shi WT, Chatterjee D, Forsberg F Characterization of Ultrasound Contrast Microbubbles Using *In Vitro* Experiments and Viscous and Viscoelastic Interface Models for Encapsulation. *J Acoust Soc America* (2005) 118(1):539–50. doi:10.1121/1.1923367

Conflict of Interest: The authors declare that the research was conducted in the absence of any commercial or financial relationships that could be construed as a potential conflict of interest.

Publisher's Note: All claims expressed in this article are solely those of the authors and do not necessarily represent those of their affiliated organizations, or those of the publisher, the editors and the reviewers. Any product that may be evaluated in this article, or claim that may be made by its manufacturer, is not guaranteed or endorsed by the publisher.